Vol. 9 | November 2015

www.lpr-journal.org

LASER & PHOTONICS REVIEWS

Numerical methods for nanophotonics: standard problems and future challenges

Benjamin Gallinet, Jérémy Butet, and
Olivier J. F. Martin

WILEY-VCH

LASER
& PHOTONICS
REVIEWS

Laser Photonics Rev. **9,** No. 6, 577–603 (2015) / **DOI** 10.1002/lpor.201500122

REVIEW ARTICLE

Abstract Nanoscale photonic systems involve a broad variety of light–matter interaction regimes beyond the diffraction limit and have opened the path for a variety of application opportunities in sensing, solid-state lighting, light harvesting, and optical signal processing. The need for numerical modeling is central for the understanding, control, and design of plasmonic and photonic nanostructures. Recently, the increasing sophistication of nanophotonic systems and processes, ranging from simple plasmonic nanostructures to multiscale and complex photonic devices, has been calling for highly efficient numerical simulation tools. This article reviews the state of the art in numerical methods for nanophotonics and describes which method is the best suited for specific problems. The widespread approaches derived from classical electrodynamics such as finite differences in time domain, finite elements, surface integral, volume integral, and hybrid methods are reviewed and illustrated by application examples. Their potential for efficient simulation of nanophotonic systems, such as those involving light propagation, localization, scattering, or multiphysical systems is assessed. The numerical modeling of complex systems including nonlinearity, nonlocal and quantum effects as well as new materials such as graphene is discussed in the perspective of actual and future challenges for computational nanophotonics.

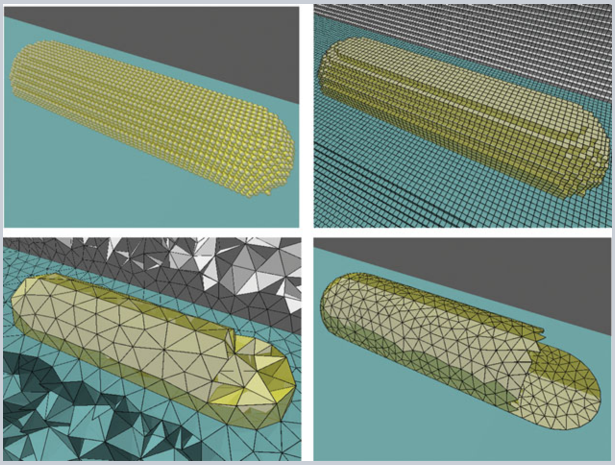

Numerical methods for nanophotonics: standard problems and future challenges

Benjamin Gallinet[1,*], **Jérémy Butet**[2], **and Olivier J. F. Martin**[2]

1. Introduction

1.1. Recent progress in nanophotonics

Light is probably the most common way we interact with our environment and, over the centuries, the human kind has developed increasingly sophisticated techniques to master it. This is not an easy task, since light tends to escape and propagate *ad infinitum*. Even with a sophisticated lens system, it is impossible to confine light over dimensions much smaller than about one wavelength, the so-called Abbe diffraction limit [1]. The first attempts to tame light and confine it to a small volume to achieve new functionalities are certainly associated with the development of the laser, where a cavity is used both to maintain light in a gain medium and to define a narrow spectral linewidth [2]. In the second half of the twentieth century, tremendous progress in semiconductor technology made possible the miniaturization of lasers, opening up the field of optoelectronics [3]. Microcavities with a well-controlled geometry are able to produce extremely strong fields and very narrow optical resonances, leading to very high quality factors Q. These have been instrumental to the development of cavity quantum electrodynamics [4, 5] and more recently cavity optomechanics [6].

Driven by analogies with semiconductors and their band structure, photonic crystals have seen extremely vivid developments, leading to a broad variety of nanophotonic structures to guide and manipulate light at the microscale and nanoscale [7, 8]. These structures rely on high-refractive-index materials and can reach quality factors in excess of $Q = 10^5$ [9]; they also open new possibilities in photonics, e.g. by controlling the group velocity of optical signals [10]. While it is possible to confine light inside cavities over dimensions comparable to the wavelength, the direct observation of such highly confined fields is also precluded by the Abbe diffraction limit and nanophotonic systems have also been used to break this imaging limit, especially in the context of near-field optical microscopy [11], where optical probes are used to record the light confined around nanostructures with sub-wavelength dimensions [12].

Over the last decade, plasmonic materials have also emerged as a popular way of producing strongly confined optical fields through the resonant excitation of free electrons in metals [13]. These structures are often described as open cavities, since light confinement occurs at the interface outside the metal. Contrary to dielectric cavities, plasmonic materials have significant losses associated with the metal and exhibit only moderate Q-factors. However,

---

[1] CSEM SA, Muttenz, Switzerland
[2] Nanophotonics and Metrology Laboratory, Swiss Federal Institute of Technology (EPFL), Lausanne, Switzerland
*Corresponding author: e-mail: benjamin.gallinet@csem.ch

they are still very useful for exploring a broad variety of physical effects, mainly because the mode volume V associated with a plasmonic nanostructure is much smaller than that of a dielectric resonator [14]. Hence, the Purcell factor $F_P \approx Q/V$, which dictates the interaction between the (open) cavity and emitters, can still be very significant [15]. Finally, plasmonic nanostructures form a very versatile platform for developing sensing applications that rely on the high sensitivity of the plasmon resonances to minute changes in their environment [16].

More recently, another family of nanophotonic components has emerged: metasurfaces [17]. These systems are composed of artificial atoms – usually plasmonic nanostructures – often organized in a periodic lattice on a surface. By virtue of the optical resonances supported by each atom, the phase of the incident light can be manipulated, producing a whole wealth of original optical effects, including negative refraction [18], complex optical beams [19], and holograms [20].

From the preceding, we see the emergence of specific electromagnetic features for nanophotonic systems: they can incorporate a broad variety of materials, not only the entire range of dielectric materials including high-index semiconductors, but also metals with losses and materials with gain, as well as anisotropic materials; they can combine geometrical features ranging from millimeter dimensions (e.g. a waveguide) down to a few nanometers (e.g. a plasmonic nanostructure); nanophotonic structures can be composed of individual elements or of periodic structures, like for example in many metasurfaces; finally, the dynamic range of the electromagnetic field in these structures can span several orders of magnitude, with the amplitude of the electric field going from zero to several hundreds over a few nanometers at the edge of a plasmonic nanostructure, for example. Experimentally relevant optical effects arising in those systems are plentiful, including both the linear and nonlinear regimes and often coupling to other physical effects, such as thermal or electronic effects, to name just two. All in all, these characteristics make the accurate and efficient modeling of nanophotonic systems extremely challenging, but also of utmost importance for the analysis and the development of new components and devices.

1.2. Modeling of nanophotonic systems

Nanophotonic systems come in a broad variety. In general, their physical description is associated with one or several observables or figures of merit which are critical for their understanding and design, such as the electric field distribution in a photonic cavity or the scattering cross section of a nanoparticle. Numerical methods have been developed to model the physical behavior of complex nanophotonic systems for which no analytical solution is available. They rely in particular on the process of discretization, which is defined here as approximating the physical problem using a set of appropriate analytical functions defined on a finite or infinite domain. An algorithm is then used to compute the solution of the approximated problem (for example a linear system of equations). The required computational memory and time depend on the problem and the chosen approach to solve it. Many popular methods have been extensively reviewed in the framework of computational electromagnetics (e.g. Refs. [21,22]), some of them having been quantitatively compared or benchmarked with analytical or experimental results in the field of nanophotonics [23–28]. However, it remains challenging to find practical cases that can fairly benchmark the different numerical methods. The approach used to generate the approximated problem strongly determines the strengths and weaknesses of the numerical method, and as a consequence the kind of problems for which it is best suited. In addition, the efficiency of a numerical method also includes many different aspects besides the computation time and memory requirements: among them, ease of implementation, complexity of discretization, and versatility. Some methods can be used to calculate a broad range of systems, while others are very efficient for specific problems. Furthermore, for the user scientist or engineer, a trade-off between the problem to solve and the method at hand usually has to be found. For these reasons, the approach chosen in this review is first to identify categories of nanophotonic problems which can be seen as fundamental building blocks for modeling nanophotonic systems, and then discuss the suitability of numerical methods to these categories. We distinguish four categories of problems: those involving light propagation, light localization, light scattering, or multiscale problems. We define the categories and introduce some potential challenges for their numerical modeling. Some examples, possibly involving experiments, are chosen from the literature to motivate the discussion. Figure 1 represents some particular occurrences in each category.

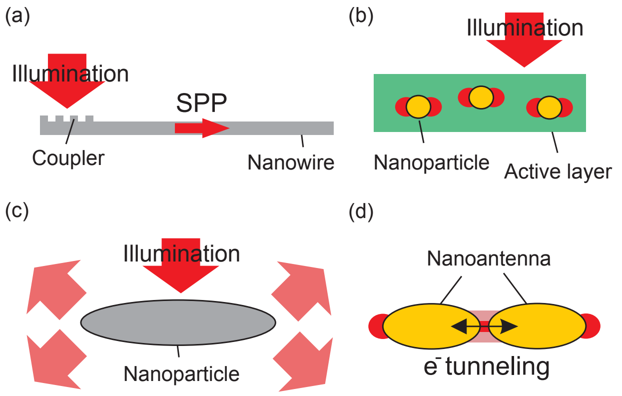

Figure 1 Examples of nanophotonic systems and applications. Red arrows and areas represent light propagation and hot spots, respectively. (a) Coupling and propagation of surface plasmon polaritons in nanowires. (b) Nanoparticles in the active layer of a solar cell to enhance light localization and harvesting. (c) Scattering and re-emission from a nanoparticle. (d) Nanoantenna with sub-nanometer gap with electron tunneling.

1.2.1. Problems based on light propagation

This first category of problems involves calculations in a one- or two-dimensional sub-diffraction limited light confinement. This can include waveguides, nanowires, or arrays of nanoparticles which support the propagation of surface plasmon polaritons (SPPs) (Fig. 1a) [29]. An example of a plasmonic waveguide is shown in Ref. [30]: an SPP is coupled into a thin silver stripe and its propagation properties are measured with a near-field scanning optical microscope. The propagation in waveguides can be enhanced by the use of specific substrates such as Bragg mirrors or photonic crystals [31]. The coupling elements can include gratings or Y-couplers [32]. In such systems, the propagation properties of light need to be evaluated in view of the future integration of components in photonic circuits: in particular, the waveguide modes are studied through their resonance frequency, field distribution, and propagation losses [33, 34]. Another important figure of merit is the coupling efficiency between circuit elements. The source can be modeled as, for example, a point-source emitter or a propagating waveguide mode. These waveguides are usually modeled in a closed (i.e. spatially limited) or quasi-open environment (e.g. to study radiation leakage of guided light in an infinite environment).

1.2.2. Problems based on light localization

One important property of some nanophotonic systems lies in the three-dimensional confinement of light below the diffraction limit, possibly with resonant effects. An insight into the near-field distribution and more generally the modal decomposition is the key enabler for the understanding and design of efficient systems such as low-threshold lasers [35] or sensors with a high signal-to-noise ratio [36]. Studies of the near field can include the calculation of the different modes, including their resonance frequencies and field distribution. An example is shown in Fig. 1b: the hot spots of the electromagnetic field around the nanoparticles upon sunlight illumination enhance the absorption in an active layer. Examples include optoelectronic devices such as solar cells or photodetectors which can be enhanced by the localization of light in the active material [37–39] and thermal [40–42] or near-field imaging [30] devices. The study of spontaneous emission in proximity to a nanostructure involves the calculation of the local density of optical states and the far-field radiation leakage pattern of a dipole emitter [35]. Efficient sensors such as gas sensors [43] or biological sensors based on surface-enhanced Raman scattering (SERS), surface-enhanced infrared absorption, fluorescence, or nanoscale refractive index variations rely on the confinement of the electromagnetic field in specific regions of space [36].

1.2.3. Problems based on light scattering or emission

This class of problems involves the interaction between a nanostructure and propagating light waves. In scattering experiments, the optical response of a nanostructure upon a given illumination is measured. As the distance between the source, the detector, and the target is usually orders of magnitude larger than the characteristic dimensions of the scatterer, the environment can be modeled as an infinite homogeneous background. Some examples can include a nanoparticle embedded in a dielectric material (Fig. 1c), placed on a substrate or on a multilayered medium such as a Bragg reflector. The response of an individual nanoparticle is usually characterized by its scattering, absorption, and extinction cross sections [44]. A large category of problems include arrays of nanostructures with various sizes. In periodic systems, the observables are the reflection, transmission, and absorption coefficients. An example of reflective surfaces is shown in Ref. [45]: here, plasmonic nanostructures are used to generate structural colors. The optical properties of the structured surface are tailored to generate a variety of colors towards a realistically rendered image. Structural colors can be also generated from high-refractive-index nanoparticles [46] or nanowires [47]. In the design of nanoantennas or metasurfaces, an in-depth design of the angular emission pattern, including the field phase and intensity, is also necessary [17, 48]. As another example, in Ref. [49] electron energy loss spectroscopy (EELS) measurements are compared to simulations of electron scattering on nanoparticles: this is usually modeled by considering a fast-moving dipolar light source.

1.2.4. Multiscale problems

A large quantity of recently developed nanophotonic systems require a modeling approach beyond the linear constitutive relations for the electric and magnetic fields or even Maxwell's equations themselves. This is the case for example for magneto-optical systems [50] or nonlinear optical effects such as second harmonic generation (SHG) or third harmonic generation (THG) in plasmonic nanostructures [51]. In active and optoelectronic devices such as light-emitting diodes, organic light-emitting diodes, lasers, or solar cells, the electronic behavior needs to be modeled together with the optical behavior [35, 38, 39]. For another class of systems where the size of the plasmonic structures is comparable to the mean free path of electrons (e.g. Fig. 1 d showing a dipole nanoantenna with a deep sub-wavelength gap), an in-depth knowledge of the dynamics of the material is required, with even in some cases fully quantum mechanical calculations [52]. In the case of nanostructured graphene, the two-dimensional nature of the material requires an accurate description of the electronic band structure prior to the study of the plasmonic modes [53]. In nanoparticle-enhanced photochemistry, charge carriers are excited on the metal surface and used to activate chemical bonds and chemical transformations in an adsorbate: an understanding of the mechanisms will in general require knowledge of the energy levels and interactions in the nanoparticle–adsorbate system [54].

1.3. Outline

Four categories of problems are identified in Section 1.2 and form together a basis for the modeling of nanophotonic systems: problems involving light propagation, localization, scattering, or multiscale problems. This review is organized in two main sections. Section 2 is dedicated to problems which can be numerically modeled by discretizing Maxwell's equations and the linear constitutive relations for the electric and magnetic fields. The currently most popular methods are reviewed: for each method, the main equations are introduced and latest examples of applications or developments in nanophotonics are provided, with the goal of illustrating their respective strengths and weaknesses. However, it is beyond the scope of this review to give a detailed description of the methods or to quantitatively compare their efficiency, for which well-documented books or review articles are cited in the text. Among the most popular methods, two main categories can be distinguished: differential and integral methods. Popular differential methods discretize the differential form of Maxwell's equations in a finite space. They include the finite differences in time domain (FDTD) and the finite element (FE) methods, as well as hybrid methods. Volume or surface integral methods restrict the discretization to the nanostructure and make use of the Green's dyadic function to compute the solution. Hybrid methods combine advantages of several methods together, which broadens their field of applications. Some popular methods based on scattering and transfer matrices are also discussed. Finally, the advantages and limits of the different numerical methods are assessed in this context.

Section 3 reviews specific examples of nanophotonic systems for which numerical simulations require models beyond the classical nature of Maxwell's equations and the linear form of the constitutive relations for the electric and magnetic fields, usually with a more accurate description of the materials at the nanoscale. This comes together with an increased complexity of implementation and requires the use of state-of-the-art methods or the development of novel tailor-made techniques. In particular, nonlinear optical effects, the nonlocal correction to the permittivity of nanostructures, and the field of quantum plasmonics are discussed. Finally, the rapidly growing field of modeling of graphene plasmonics is reviewed.

1.4. Target audience

This review is aimed at providing engineers and experimental researchers in nanophotonics with a basic knowledge of the advantages and limitations of numerical methods. Some fundamental equations of the methods as well as applications or developments in the recent literature are selected in order to provide the reader with the ability to make an informed choice of the method that is the most appropriate to the problem at hand.

Researchers in computational nanophotonics will also find a review of the latest developments in the field through selected publications, as well as a discussion of the future possible directions in developing new methods or improving the existing ones. The far-reaching goal of this community is to enable the use of multiscale and highly versatile numerical methods that are able to efficiently handle arbitrary large and multiscale systems.

2. Numerical methods based on classical Maxwell's equations

In this section, each method is briefly described through its fundamental equations in order to give an intuitive understanding of the type of problem for which it is best suited. The emphasis is put on classical numerical methods that are designed to handle a relatively broad variety of systems: the so-called differential and integral methods. This description is supported by application examples from the recent literature. At this point, it must be mentioned that an exhaustive list of examples illustrating every particular feature of the methods would practically be impossible, given the variety of methods and existing nanophotonic systems. Here, the examples are selected because they either clearly illustrate an advantage or limitation of a given method, or highlight cases where simulations could model successfully an experimental result, or bring a new layer of understanding of a particular effect.

Differential methods solve Maxwell's equations in their differential form. They rely on a volume discretization in a finite computational domain. A first approach consists of directly discretizing Maxwell's equations in time and space using finite differences: this is the core of the FDTD method which is discussed in Section 2.1. On the other hand, the FE method in Section 2.2 consists of expanding the electromagnetic fields as local functions in elements, which results in higher accuracy in the frequency domain. Its extension to the time domain is discussed in Section 2.3, together with the discontinuous Galerkin time-domain (DGTD) method. Integral methods transform Maxwell's equations in an integral form through the use of the Green function and discretization is reduced to the nanostructured objects. A first approach consists of restricting the discretization of the problem to the volume of the objects. These methods are usually called volume integral equation (VIE) methods and are reviewed in Section 2.4. On the other hand, for piecewise homogeneous objects, the discretization can be further reduced to the surface boundaries. The methods using these approaches are called surface integral equation (SIE) methods and are reviewed in Section 2.5. In Section 2.6, hybrid methods and geometry-specific methods such as the T-matrix method, the rigorous coupled wave analysis (RCWA), or semi-analytical methods are discussed. For further details on the implementation of these methods, the reader is referred to the related books or review articles. The summary (Section 2.7) takes the form of a table evaluating the methods and their compatibility with the different nanophotonic problems identified in Section

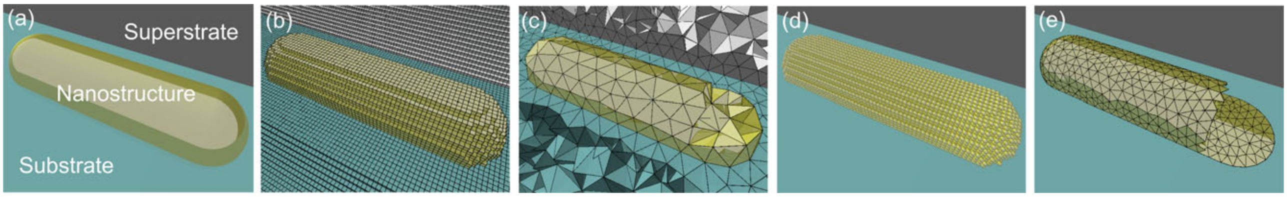

Figure 2 Examples of discretization for computational modeling of an optical nanoantenna. (a) Sketch of the nanostructure sandwiched between a substrate (e.g. a quartz wafer) and a superstrate (e.g. air). (b) Finite differences in time domain method, with discretization in the nanostructure, the substrate, and the superstrate using a Cartesian grid. (c) Finite element or discontinuous Galerkin time domain method, with discretization of the nanostructure, the substrate, and the superstrate using tetrahedral elements. (d) Discrete dipole approximation, with discretization in dipoles inside the nanostructure. (e) Surface integral equation method, with discretization in triangular elements at the surface of the nanostructure.

1.2: problems based on light propagation, localization and scattering.

2.1. Finite differences in time domain

The FDTD method is one of the most popular methods in nanophotonics because of its ability to handle a large variety of problems [55]. In this method, both time and space are discretized, i.e. all spatial and temporal derivatives in Maxwell's curl equations are replaced by finite difference quotients[21, 56]. In Fig. 2b, an example of discretization of a metallic nanoantenna on a substrate in the framework of FDTD is shown. The respective volumes of the nanostructure, the substrate, and the superstrate are represented by a staircase approximation. The popular algorithm introduced by Yee [57] is briefly shown here; a more detailed account can be found in, for example, Refs. [21, 55, 56].

In the presence of source currents $\mathbf{J}$ and charges ρ, Maxwell's equations in their differential form are given by

$$\nabla \times \mathbf{H} = \frac{\partial \mathbf{D}}{\partial t} + \mathbf{J} \tag{1}$$

$$\nabla \times \mathbf{E} = -\frac{\partial \mathbf{B}}{\partial t} \tag{2}$$

$$\nabla \cdot \mathbf{D} = \rho \tag{3}$$

$$\nabla \cdot \mathbf{B} = 0. \tag{4}$$

In the Yee algorithm, a Cartesian grid of rectangular cells with side lengths Δx, Δy, Δz for the spatial discretization and a time step Δt for the temporal discretization are chosen. Faraday's law without current is considered as an example (Eq. (2)). The same procedure can be directly applied to Ampere's law (Eq. (1)) and to the introduction of current sources at specific points of the grid. Introducing the notation $\mathbf{E}(x, y, z, t) = \mathbf{E}^n(j, k, l)$, where $x = j\Delta x$, $y = k\Delta y$, $z = l\Delta z$, $t = n\Delta t$, $j, k, l, n \in \mathbb{N}$, one obtains the discretization of the x-component of Eq. (2):

$$\begin{aligned} B_x^{n+1/2}\left(j+\frac{1}{2}, k, l\right) &= B_x^{n-1/2}\left(j+\frac{1}{2}, k, l\right) \\ &\quad - \frac{\Delta t}{\Delta y}\left[E_z^n\left(j+\frac{1}{2}, k+\frac{1}{2}, l\right) - E_z^n\left(j+\frac{1}{2}, k-\frac{1}{2}, l\right)\right] \\ &\quad + \frac{\Delta t}{\Delta z}\left[E_y^n\left(j+\frac{1}{2}, k, l+\frac{1}{2}\right) - E_y^n\left(j+\frac{1}{2}, k, l-\frac{1}{2}\right)\right]. \end{aligned} \tag{5}$$

Equation (5) implies that the magnetic field at the time increment $n + 1/2$ is updated from the magnetic field at time increment $n - 1/2$ and the electric field at time increment n in a leapfrog manner. This procedure can be easily generalized to the other components of Eq. (2) where the electric field at time increment $n + 1$ is updated from the electric field at time increment n and the magnetic field at time increment $n + 1/2$. This way, the electromagnetic field can be computed at all time over the computational grid. Only Ampere's and Faraday's laws are explicitly time-stepped, because the Gauss laws (Eqs. (3) and (4)) are enforced implicitly with this FDTD approach.

In general, the permittivity undergoes spatial variations within a grid cell: the permittivity in each cell is then calculated as an average value, following, for example, the Maxwell–Garnett rule for dielectric materials [21]. The size of the discrete cells is critical for achieving a sufficiently high numerical accuracy. It is usually recommended that the spatial increment Δx, Δy, and Δz should not be larger than $\lambda/20$, where λ denotes the wavelength of the incident wave [21]. In order to ensure a stable numerical result, the time increment should in addition satisfy the Courant condition given by [56]

$$c_0 \Delta t \leqslant \frac{1}{\sqrt{\frac{1}{\Delta x^2} + \frac{1}{\Delta y^2} + \frac{1}{\Delta z^2}}}. \tag{6}$$

It was recently shown that the time increment should be as large as possible, but within the Courant limit [58]. As can be seen in Eq. (5), the Yee algorithm uses an orthogonal uniform grid. It is second-order accurate by nature of the central-difference approximation used to realize the first-order spatial and temporal derivatives. However, such a simple approach can yield numerical inaccuracies of various kinds: (1) when the space increment is not small enough to resolve the high field gradients in particular regions of space, for example in a resonant cavity; (2) when the position of the cell does not follow the shape of the material boundaries, resulting in a staircase representation and implementation for complex geometries. Among the approaches that can enhance the spatial resolution, one can cite the use of a nonhomogeneous grid [59] or the generalization of the Yee algorithm to irregular nonorthogonal unstructured grids [60]. As electromagnetic fields can reach high gradients around nanophotonic resonators, great attention must be given to the modeling of such materials for accurate and reliable results [55]. Another challenge related to the FDTD gridding arises from its numerical dispersion. The numerical phase velocity of waves depends on the propagation direction, which can be problematic for long-range propagation. This source of inaccuracy can be reduced if a sufficiently fine gridding is chosen, or with the use of mitigation algorithms [56]. Only the field from the previous time step is needed to compute the new field. Thus, the required computational memory scales only with the volume of the computational domain, which makes FDTD efficient for large systems. The number of numerical operations in FDTD scales with the fourth power of the particle size [21, 61].

The implementation of time-domain methods to periodic systems has fundamental limitations arising from the periodic boundary conditions. Valid results can be obtained at normal incidence (i.e. when there is no phase delay between cells), but oblique incidence requires using the field components backwards and forwards in time. Some methods have been introduced to mitigate this fundamental limitation, among which are those applying a field transformation to eliminate the time delay across the FDTD grid with a supplementary computational cost [56].

In numerical methods based on the differential form of Maxwell's equations, boundary conditions are applied to the fields. They can be of several types: Dirichlet, von Neumann, or their combination. Also, in systems with discrete symmetry, some nontrivial symmetry-driven boundary conditions can be enforced on truncated domains [62]. For the case of theoretically infinite environments where the Sommerfeld radiation condition is applied to the fields (e.g. for scattering or radiation problems), the finite memory allocation means that the computational domain must still be finite. The boundary should reproduce as accurately as possible a homogeneous nonlossy infinite medium, i.e. nonphysical reflections must be minimized. Absorbing boundary conditions were introduced, but they have the limitations of residual reflections depending on the frequency and the incidence angle [56, 63]. In order to solve this problem, the perfectly matched layer (PML) was introduced [64], which is a layer of lossy material with a perfectly matched interface that does not reflect a plane wave for all frequencies and all angles of incidence and polarizations. PMLs can be seen either as coordinate stretching in the frequency domain [66] or as an artificial anisotropic absorbing medium [67]:

$$\underline{\underline{\varepsilon}} = \underline{\underline{\Lambda}}\varepsilon,\ \underline{\underline{\mu}} = \underline{\underline{\Lambda}}\mu,\ \underline{\underline{\Lambda}} = \begin{pmatrix} \frac{s_y s_z}{s_x} & 0 & 0 \\ 0 & \frac{s_x s_z}{s_y} & 0 \\ 0 & 0 & \frac{s_x s_y}{s_z} \end{pmatrix}, \tag{7}$$

where the PML parameters s_j $(j = x, y, z)$ are chosen as $s_j(\omega) = 1 - \sigma_j/(i\omega)$ and σ_j controls the damping of a wave propagating along the i-direction. Further designs of the PML parameters can be implemented to accelerate the decay of propagating or evanescent waves [56, 63]. Special care should be taken with the use of PMLs, because numerical reflection errors can alter the numerical accuracy. Furthermore, the PML approach breaks down when the distribution of the permittivity at the edges of the computational domain is not homogeneous in the direction perpendicular to the PML, such as a waveguide entering a PML with an angle [68]; in such cases, the use of absorbing boundary conditions is recommended.

Some materials that can be found in photonic nanostructures such as metals or semiconductors are dispersive. In particular, the dispersion of a metallic material determines the plasmon resonance frequency and markedly affects the optical properties [69]. In numerical simulations, a frequency-dependent dielectric permittivity is included to account for this effect, which can be evaluated for instance with the Drude model or from experimental data. An example of a frequency-dependent dielectric function is illustrated in Fig. 3, where a quantum dot nanocrystal of CdSe is placed in the gap of a pair of silver nanoparticles. A single Lorentzian peaked at the quantum dot's resonance frequency is considered for modeling its permittivity. The real-valued time-domain susceptibility function $\chi(t)$ is obtained by inverse Fourier transformation. At any point in a linearly dispersive medium, the time-dependent electric flux density is calculated from the electric field intensity. This implies in particular that the electric flux takes its value from the history of the system. In time-domain methods, the implementation of such dispersive materials is not straightforward. A popular approach is the piecewise-linear recursive convolution method [70]. In order to avoid the storage of field values at all times, the piecewise-linear recursive convolution method introduces a time-dependent vector variable (the recursive accumulator). At each time step, the accumulator and the fields are updated recursively from the previous time step. Another method consists of adding an auxiliary differential equation in the time domain linking the polarization and the electric flux density: an example of application to the multi-term Debye and Lorentz models is shown in Ref. [71].

Another challenge concerns the efficient computation of scattering from long-duration pulses or plane waves. The total field/scattered field technique, popular in FDTD [72],

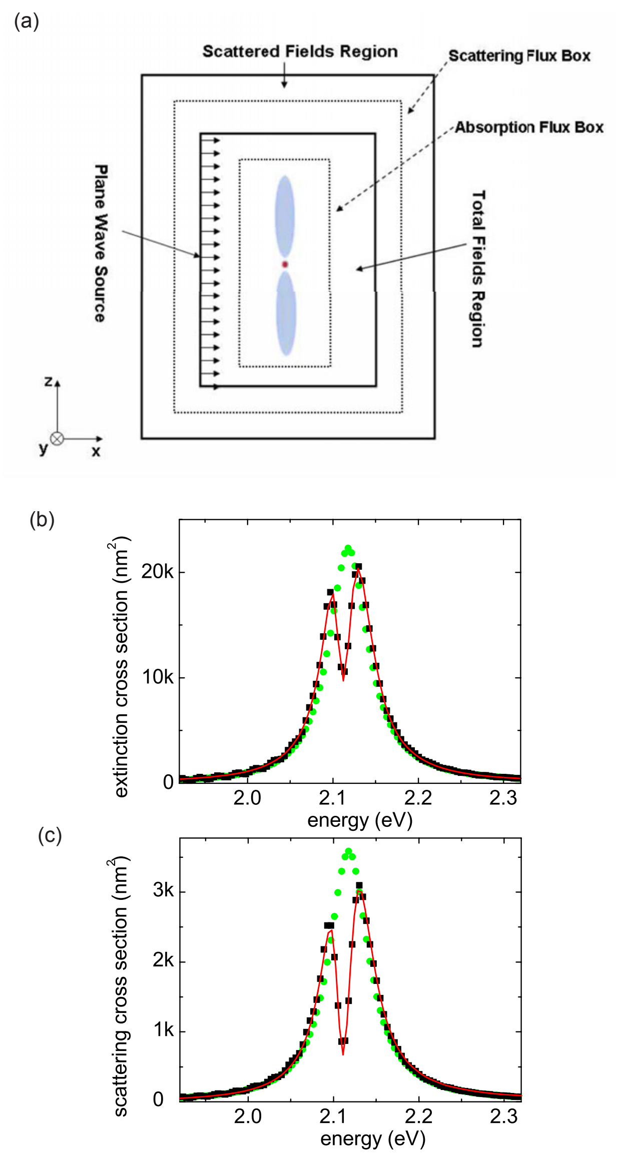

Figure 3 Simulation of scattering and extinction cross sections of a quantum dot–metal nanoparticle hybrid system using FDTD. (a) Geometry of the system with domains used for the simulations. The blue ellipses represent silver nanoparticles and the red circle represents a semiconductor nanocrystal. In (b) and (c), solid black squares are values of extinction and scattering cross sections ($\times 10^3$ nm^2), respectively. The quantum dot linewidth is 10 meV. The solid lines are fits to a phenomenological coupled-oscillator model. Solid circles are extinction and scattering spectra for the same system but without quantum dot absorption, also calculated by the FDTD method. Adapted from Ref. [248] with permission. Copyright (2010) Optical Society of America.

splits the electromagnetic fields into two contributions, the incident and scattered fields. If the incident field is a plane wave, the time iteration is continued until the fields have converged to a steady-state solution. As an illustration in Fig. 3, a time-windowed plane wave is incident on a structure, where it is absorbed and scattered. The computational domain includes a region containing the scattering where the total field is computed using the FDTD algorithm and a region where only the scattered field is computed. The plane where the wave is generated defines the interface between the total-field and scattered-field regions. The absorption spectrum is obtained by taking the Fourier transform of the flux through a three-dimensional box around the structure in the total-field region and the scattering spectrum is obtained by taking the Fourier transform of the flux through a three-dimensional box around the structure in the scattered-field region.

The far field can also be accurately computed from the numerically computed near field without the need of extending the computation grid [56]: with this technique called the near- to far-field transformation, the Green theorem is applied on surface currents that are calculated at the boundaries of the computational domain. In order to obtain the far-field properties of a system, a pulse can be used as an incident field and the Fourier transform of the field can be calculated, which yields an entire spectrum in a single calculation [56]. This approach requires nevertheless continuing the time iteration until the field values have decayed below a given threshold value and is limited in accuracy for resonators with high quality factors which decay slowly with time.

Finally, time-domain methods such as FDTD can cover calculations of light propagation in a natural way. Propagation lengths and radiative as well as nonradiative losses can be assessed in a variety of nanoscale waveguides made for instance from nanowires [33], arrays of nanoparticles [73], or nanobelts [74]. In Fig. 4, FDTD calculations were performed to determine the propagation lengths of SPPs in gold nanowires. The calculations could first reveal that several modes were supported by the nanowires, as indicated by the surface charge distribution. A Gaussian beam with a fixed wavelength was normally incident and focused on the ends of the nanowires. SPP propagation lengths for different nanowires and polarizations were determined from linear fits to semilog plots of the time-averaged energy flow (Poynting vector) along the nanowire length as a function of distance. It is also discussed in this example that the cross-sectional shape of the nanowires and the charge distribution of the modes play an important role in their respective propagation lengths. Apart from commercial softwares, Meep [75] is an example of FDTD open source code.

2.2. Finite elements

The FE method is another popular differential method in nanophotonics, which allows for accurate computation of the electromagnetic field originally in the frequency domain. Hybrid and time-domain methods based on FEs include the finite elements in time-domain method (FETD) and the DGTD method. A detailed account of their implementation and various features can be found in Ref. [63].

A linear dependence of the magnetic and electric polarizations is assumed. Eliminating the magnetic field with the

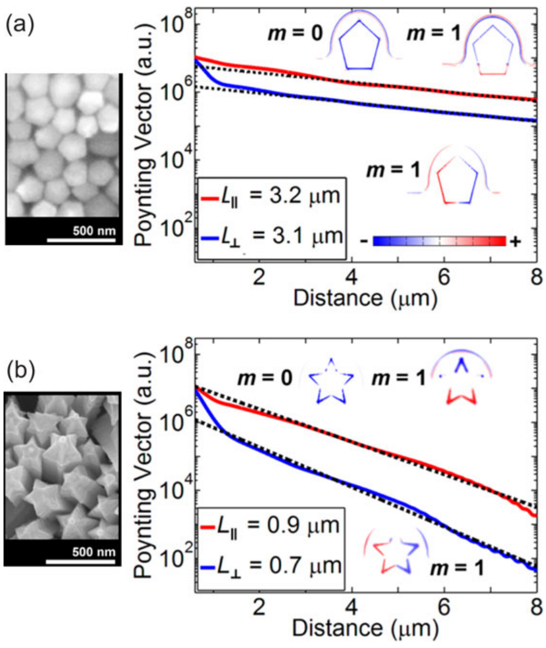

Figure 4 SPP propagation lengths in gold nanowires calculated with FDTD for longitudinal and transverse polarized excitations. The propagation lengths were obtained from fitting the decay profiles. (a) Pentagon cross section. (b) Star cross section. Insets: scanning electron microscopy images of the chemically synthesized nanowires and computed surface charge distribution. Adapted with permission from Ref. [33]. Copyright (2014) American Chemical Society.

aid of the constitutive relations, the vector wave equation is obtained from Maxwell's equations:

$$\nabla \times \left(\frac{1}{\mu}\nabla \times \mathbf{E}\right) + \varepsilon\frac{\partial^2 \mathbf{E}}{\partial t^2} + \sigma_{\mathrm{e}}\frac{\partial \mathbf{E}}{\partial t} = -\frac{\partial \mathbf{J}}{\partial t}, \qquad (8)$$

where μ is the magnetic permeability, ε the electric permittivity and σ_{e} the electrical conductivity. For time-harmonic fields, an exponential time dependence in $e^{-i\omega t}$ is assumed. Maxwell's equations with an electric current source **J** can be combined to yield the electric field wave equation in the frequency domain:

$$\nabla \times \left(\frac{1}{\mu_{\mathrm{r}}}\nabla \times \mathbf{E}\right) - k_0^2\varepsilon_{\mathrm{r}}\mathbf{E} = ik_0Z_0\mathbf{J}, \qquad (9)$$

where μ_{r}, ε_{r}, k_0, and Z_0 are the relative permeability, relative permittivity, free space wavevector, and impedance, respectively. The solution of the electric field wave equation (Eq. (9)) with current is sought, in combination with the general boundary conditions:

$$\frac{1}{\mu_{\mathrm{r}}}\hat{n} \times (\nabla \times \mathbf{E}) + \gamma_{\mathrm{e}}\hat{n} \times (\hat{n} \times \mathbf{E}) = \mathbf{U}, \qquad (10)$$

where γ_{e} is a known parameter and **U** a known vector. The following functional is considered:

$$\begin{aligned} F(\mathbf{E}) = \frac{1}{2}\int_V \left[\frac{1}{\mu_{\mathrm{r}}}(\nabla \times \mathbf{E})\cdot(\nabla \times \mathbf{E}) - k_0^2\varepsilon_{\mathrm{r}}\mathbf{E}\cdot\mathbf{E}\right]\mathrm{d}V \\ + \int_S \left[\frac{\gamma_{\mathrm{e}}}{2}(\hat{n} \times \mathbf{E})\cdot(\hat{n} \times \mathbf{E}) + \mathbf{E}\cdot\mathbf{U}\right]\mathrm{d}S \\ - ik_0Z_0\int_V \mathbf{E}\cdot\mathbf{J}\,\mathrm{d}V. \qquad (11) \end{aligned}$$

Seeking for the stationary point of the functional with respect to the electric field ($\delta F = 0$) is equivalent to solving the boundary value problem involving Eqs. (9) and (10). Note that a functional for anisotropic media can be derived in an equivalent way as in Eq. (11).

The domain V on which the problem is defined is then separated in a set of elements and the electric field is expanded in each element on a set of basis functions. Tetrahedral and hexahedral elements are flexible and can model accurately material boundaries (Fig. 2c). As a differential method, the entire computational domain has to be discretized: this includes in the example of Fig. 2c the nanostructure, the substrate, and the superstrate. Seeking the stationary point of the function in Eq. (11) can lead to solutions that do not fully satisfy the divergence condition called spurious solutions (Eqs. (3) and (4)), as well as to difficulties in imposing boundary conditions and treating field singularities at edges and corners. Edge elements with vector basis functions $\mathbf{N}_j$ were introduced to solve these issues: these basis functions enforce continuity of the fields and their curl, and therefore implicitly satisfy Gauss' laws. The electric field is expanded as

$$\mathbf{E} = \sum_{j=1}^{N} E_j\mathbf{N}_j(\mathbf{r}), \qquad (12)$$

where N is the number of unknowns, corresponding to the number of edges, and E_j are the unknown coefficients. Using the decomposition of Eq. (12), the variational problem $\delta F = 0$ becomes

$$\sum_{j=1}^{N} M_{jk}E_k = b_j, \qquad (13)$$

where

$$\begin{aligned} M_{jk} = \int_V \frac{1}{\mu_{\mathrm{r}}}\left[(\nabla \times \mathbf{N}_j)\cdot(\nabla \times \mathbf{N}_k) - k_0^2\mathbf{N}_j\cdot\mathbf{N}_k\right]\mathrm{d}V \\ + \int_S \gamma_{\mathrm{e}}(\hat{n} \times \mathbf{N}_j)\cdot(\hat{n} \times \mathbf{N}_k)\,\mathrm{d}S \qquad (14) \end{aligned}$$

and

$$b_j = -\int_S \mathbf{N}_j\cdot\mathbf{U}\,\mathrm{d}S + ik_0Z_0\int_V \mathbf{N}_j\cdot\mathbf{J}\,\mathrm{d}V. \qquad (15)$$

The system of equations in Eq. (13) can be written in matrix notation:

$$\underline{\underline{M}}\,\underline{E} = \underline{b}, \tag{16}$$

where $\underline{E}$ is the vector of unknown electric field amplitudes, $\underline{b}$ is related to the source terms, and $\underline{\underline{M}}$ is a sparse matrix. The vector wave equation without source can be considered as well, resulting in the eigenvalue equation $\underline{\underline{M}}\,\underline{E} = 0$ which can be useful when calculating the eigenmodes of a nanophotonic resonator. For example, the eigenvalue in a dielectric three-dimensional cavity with Dirichlet boundary conditions is k_0^2. The calculation of eigenvalue problems using FEs can also be applied to open or lossy cavities or waveguides. It must also be mentioned that eigenvalue equations are not specific to FEs but can also be found in other methods in the frequency domain. The basis functions are polynomial functions of the position. Although the first-order basis functions show good accuracy, a higher order convergence rate can be achieved using higher order vector elements [76, 77]. As a differential method, the FE method requires the use of PMLs, an artificial separation of incident and scattered fields, as well as near- to far-field transformations which complicate the implementation and use of the method for scattering problems, as explained in Section 2.1. However, the dispersion of materials and periodic boundary conditions can be directly implemented since the FE method is in the frequency domain. Overall, the number of numerical operations in the FE method scales approximately with the seventh power of the particle size when Gaussian elimination is used, and can be brought to the fourth power with the conjugate gradient method [21]. The memory consumption scales approximately with the fifth power of the particle size.

In contrast to FDTD, the use of basis functions enables one to account for the geometry of nanostructures with a high accuracy, which can be crucial when studying the effect of nanoscale variations of shapes on the optical properties [33,78]. The high accuracy of the computed electromagnetic field allows studying the electromagnetic confinement in nanostructures and in particular the influence of geometrical parameters on the near-field distribution. This makes FE-based approaches very well suited for the simulation of systems based on light localization and their related applications [79]. Dispersive materials can also be directly implemented as the FE method is in the frequency domain. In the frequency domain, the modes as well as their resonance frequencies, losses, and area can be directly calculated, which are critical in the design of cavities for nanolasers [80, 81] (an example is shown in Fig. 5). An accurate simulation of the near field is also critical to understand and design nanostructures for optical trapping and sensing [82]. In another example, the near-field information obtained from FE calculations is used to evaluate the temperature distribution of plasmonic nanostructures using a thermal transport equation [42].

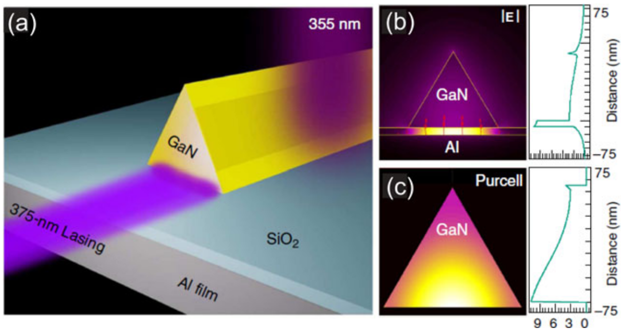

Figure 5 Near-field properties of an ultraviolet plasmonic nanolaser device computed with the FE method. (a) Schematic of the device. (b) Absolute electric field (|**E**|) distribution (left) around the plasmonic device with a wavelength of 370 nm, corresponding to the lasing wavelength of GaN nanowires. The electric field direction is indicated by red arrows. The cross-sectional amplitude (right) is also shown. (c) Calculated local Purcell factor distribution around the GaN nanowire (left) and cross-sectional Purcell factor plot (right). Adapted with permission from Ref. [81]. Copyright (2014) Nature Publishing Group.

2.3. Hybrid finite elements/finite differences, discontinuous Galerkin time-domain method

The FE method can be extended to the time domain by seeking for the stationary point of the functional corresponding to the vector wave equation (Eq. (8)). This leads to a differential equation in the time domain which can be solved for example using a finite difference scheme. Different time-stepping schemes can be adopted: the most accurate approaches (second order, central difference, and Newark methods), however, require solving a system of equations at each time step, resulting in general in higher computational costs than FDTD [63]. If linear, rectangular hexahedral elements are adopted and the spatial integrations are evaluated using the trapezoidal rule, then the FDTD algorithm is recovered [56, 83]. Hybrid methods have been recently developed in order to benefit from the advantages of both FDTD and FE methods. In particular, methods have been proposed to improve the efficiency of FETD. The dual-field domain decomposition method divides the computational domain into small sub-domains and couples the fields between the sub-domains by exchanging the surface equivalent electric and magnetic currents at the sub-domain interfaces and computes the electric and magnetic fields step by step in a leapfrog manner [84]. In the same spirit, the element-level decomposition method considers each FE as a sub-domain [85]. Techniques which use a combination of a Cartesian space lattice with a time-domain FE mesh consisting of tetrahedra and pyramids have also been developed [56,86]. Part of the computational domain which does not require fine geometrical rendering is discretized using FDTD and the update of the fields with time is made explicitly. A FE mesh is implemented on a reduced domain where accurate computation is required. In this sub-domain, the fields are updated implicitly and interfaced with the FDTD grid.

A popular method is the DGTD method [63]. A detailed review of the method and its application to nanophotonics is given by Busch *et al.* [87]. The DGTD method directly solves Maxwell's equations inside each element and connects them through a numerical flux. The discretization in the time domain can be made using the central difference method in a similar manner to FDTD. This method allows the use of higher order expansion and testing functions, providing great accuracy, while solving equations locally within each element. It therefore combines the accuracy of high-order FE methods with a time-domain description, which makes it efficient for large systems [88]. Similarly to the FDTD and FE methods and as a differential method, the DGTD method also requires the use of tailored PMLs and an artificial separation of incident and scattered field, as briefly explained in Section 2.1 and detailed in Ref. [89]. Several examples of applications for nanophotonics can be found, including nanostructured metallic films [89] and split-ring resonators [87].

Overall, the methods outlined in this section feature the typical limitations (such as the challenging implementation of periodic boundary conditions, dispersive materials, open boundary conditions, scattering by long-duration fields) and advantages (efficient simulation of large systems, calculation of explicit time-domain decays of waves) of time-domain methods. Great care has also to be taken in order to model highly resonant systems which decay slowly in time. Their advantage as compared to FDTD is their higher accuracy, which comes at the price of a more challenging implementation and generally higher computational cost.

2.4. Volume integral methods

VIE methods transform Maxwell's equations in an integral form to solve for the electromagnetic field on a reduced volume. There are different approaches for deriving the numerical equations associated with the solution of Maxwell's equations in their integral form. Here we will follow Ref. [90], starting from the vectorial wave equation and draw at the end of the section similarities with the most popular implementation of this approach, the discrete dipole approximation (DDA) [91].

Assuming nonmagnetic materials, we consider a scatterer with permittivity $\varepsilon(\mathbf{r})$ embedded in an infinite homogeneous background with permittivity ε_{b}. The scatterer does not need to be homogeneous, but can be composed of different materials, including metals with a complex permittivity; furthermore, it can also be made of anisotropic materials [92], although we consider here a scalar permittivity for simplicity. Since this approach is in the frequency domain, all calculations are performed at a single frequency ω and harmonic fields with $\exp(-i\omega t)$ are assumed. The volume integral methods presented here consider only the electric field, since it is in principle sufficient to solve any electromagnetic problem with nonmagnetic materials, as is the case for most nanophotonic systems. This represents an important difference from many other numerical methods, which usually solve simultaneously for the electric and magnetic fields. In principle, once the electric field is known for a given problem, the magnetic field can be found using Eq. (2); however, this task is not trivial with a finite differences approach, since the discretized form of Eq. (2) requires knowing the electric field on several points around the location where the magnetic field is calculated, which generates quite some computational overhead.

When this system is illuminated with an incident field $\mathbf{E}^0(\mathbf{r})$ propagating in the background medium, the total electric field (incident field plus scattered field) is a solution of the vectorial wave equation obtained from Eq. (9) in the absence of currents:

$$\nabla \times \nabla \times \mathbf{E}(\mathbf{r}) - k_0^2 \varepsilon(\mathbf{r})\, \mathbf{E}(\mathbf{r}) = 0, \tag{17}$$

where $k_0^2 = \omega^2/c^2$ is the vacuum wave number. The key step in the derivation of the VIE is to consider the scattering problem as the superposition of a problem composed of the infinite homogeneous background ε_{b} plus another problem, where the dielectric contrast,

$$\Delta\varepsilon(\mathbf{r}) = \varepsilon(\mathbf{r}) - \varepsilon_{\mathrm{b}}, \tag{18}$$

describes how the scatterer differs from that background [90]. In this way, the total electric field becomes a solution of the integral equation

$$\mathbf{E}(\mathbf{r}) = \mathbf{E}^0(\mathbf{r}) + \int_{\mathrm{V}} \mathrm{d}\mathbf{r}' \underline{\underline{G}}^{\mathrm{b}}(\mathbf{r}, \mathbf{r}') \cdot k_0^2 \Delta\varepsilon(\mathbf{r}') \mathbf{E}(\mathbf{r}'), \tag{19}$$

where the integration runs over the entire scatterer volume V and $\underline{\underline{G}}^{\mathrm{b}}(\mathbf{r}, \mathbf{r}')$ is the Green tensor associated with the background. This dyadic has a very simple interpretation. It is a 3 × 3 matrix, the columns of which represent the electric field at position $\mathbf{r}$ for three orthogonal dipoles located at position $\mathbf{r}'$: the first column corresponds to the three electric field components (E_x, E_y, E_z) for the field radiated by a dipole oriented in the x-direction (Fig. 6a); the second column gives the three electric field components radiated by a dipole oriented in the y-direction; and the third column is the field radiated by a dipole oriented in the z-direction. Consequently, in that formalism, the system is discretized by assigning to each mesh three orthogonal dipolar polarizabilities and the corresponding meshes are often represented by spheres (Fig. 2d). This approach is validated by the fact that the polarizability of a scatterer much smaller than the wavelength is essentially dipolar [93].

This physical interpretation of the Green tensor as the field produced by a dipolar source points to an intrinsic difficulty associated with this method: when the observation point $\mathbf{r}$ gets closer to the source point $\mathbf{r}'$, the field diverges (the electric field of a dipole diverges at the position of the dipole). Consequently, one must take the principal value for the integral in Eq. (19), which leads to the following discretized equation:

$$\begin{aligned} \mathbf{E}_i &= \mathbf{E}_i^0 + \sum_{j=1,\, j\neq i}^{N} \underline{\underline{G}}^{b}_{i,j} \cdot k_0^2 \Delta\varepsilon_j \mathbf{E}_j \mathrm{V}_j \\ &\quad + \mathbf{M}_i \cdot k_0^2 \Delta\varepsilon_i \mathbf{E}_i - \mathbf{L} \cdot \frac{\Delta\varepsilon_i}{\varepsilon_{\mathrm{B}}} \mathbf{E}_i, \quad i = 1, \ldots, N, \end{aligned} \tag{20}$$

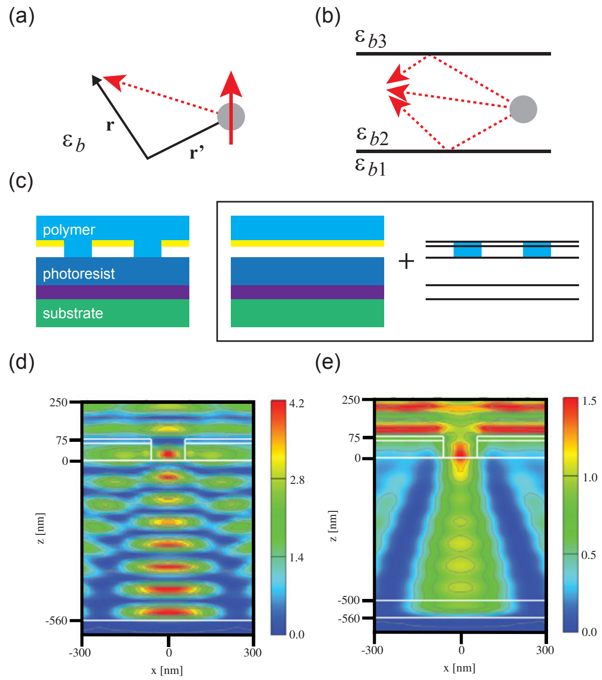

Figure 6 (a) The Green tensor used in the VIE represents the field radiated by a dipole. In free space, only direct radiation exists (dashed line), while (b) in a stratified medium, reflections at the different interfaces also exist. (c) Light scattering by scatterers in a stratified background can easily be computed using this approach. In the example, a light-coupling mask used for nanolithography is decomposed into a stratified background plus a few scatterers. (d) Intensity distribution in the photoresist for such a light-coupling mask. (e) When an additional anti-reflection layer is used above the substrate, the standing wave in the photoresist disappears. Adapted from Ref. [99] with permission. Copyright (2001) Optical Society of America.

where the discretized field $\mathbf{E}_i = \mathbf{E}(\mathbf{r}_i)$, the discretized dielectric contrast $\Delta\varepsilon_i = \Delta\varepsilon(\mathbf{r}_i)$, and the discretized Green tensor $\underline{\underline{G}}^{\mathrm{b}}_{i,j} = \underline{\underline{G}}^{\mathrm{b}}(\mathbf{r}_i, \mathbf{r}_j)$ have been introduced for the N meshes corresponding to the discretized scatterer. This discretization assumes that all these parameters are constant over one single mesh volume V_j. More refined discretization approaches have been proposed for Eq. (19), using concepts derived from signal processing [94, 95] or from the FE technique [96], although the latter case has only been implemented for two-dimensional geometries.

Since this approach relies on the discretization of the scatterer into small volumes, inhomogeneous scatterers can easily be handled and discretized into a collection of meshes with different permittivities. The accuracy of the method depends on the mesh size used for the discretization; a sufficient accuracy for most physical situations is achieved with 5 to 10 meshes per wavelength, although the convergence of the method is not always monotonic [97]. Overall, the number of numerical operations scales approximately with the ninth power of the particle size when Gaussian elimination is used, and can be brought to the sixth power with the conjugate gradient method [21] or even further down with the use of fast Fourier transform techniques [61]. The memory consumption scales approximately with the sixth power of the particle size. As a matter of fact, a limitation of this approach lies in the fact that the resulting matrix is dense, non-Hermitian, and can have a large condition number [98].

The simple interpretation of the Green tensor as the field of a collection of orthogonal dipoles illustrated in Fig. 6a prompts a very interesting extension of VIEs for light scattering in complex backgrounds, especially stratified media. For an infinite homogeneous space, the field radiated by a dipole corresponds to direct radiation from the source (at position $\mathbf{r}'$) to the field point (at position $\mathbf{r}$), as indicated by the straight radiation line in Fig. 6a. For a stratified background, e.g. composed of three different materials with permittivities $\varepsilon_{\mathrm{b}1}$, $\varepsilon_{\mathrm{b}2}$, and $\varepsilon_{\mathrm{b}3}$, in addition to this direct radiation, additional radiation paths exist with reflection at the different interfaces (Fig. 6b). These additional paths account for the entire interaction between the scatterer and its surroundings; hence, by using the Green tensor associated with such a stratified medium, i.e. the field generated by a dipole in a layered background, one can compute light scattering by a scatterer embedded into that background by merely discretizing the scatterer only [99]. For a homogeneous medium, the Green tensor $\underline{\underline{G}}^{\mathrm{b}}_{i,j}$ is analytical; this is no longer the case in a stratified background, where the Green tensor must be computed numerically – usually in the spectral domain using numerical integration in the complex plane – which has an additional, non-negligible, computational cost [100]. This approach is especially efficient when the scatterer volume is limited, compared to the volume of the stratified background, as illustrated in Fig. 6c–e. This figure shows the field distribution produced by a light-coupling mask for nanolithography [101]: the mask is made of a soft polymer and includes a thin gold layer to increase the contrast. It is applied onto the photoresist, where it produces a strongly localized field distribution, which can be used to expose sub-wavelength features [102]. The geometry is easily decomposed into a stratified background made of the different homogeneous layers, and a few localized scatterers (Fig. 6c). The numerical solution of Eq. (20) requires only the discretization of these few scatterers that link the polymer layer with the photoresist. Note that for some backgrounds, the dielectric contrast can take arbitrary values, including negative values; this is for example the case when one simulates light scattering by air bubbles within a dielectric background, leading to $\Delta\varepsilon < 0$. The role played by the background in that type of simulation is illustrated in Fig. 6d and e, which show two simulations with exactly the same scatterers accounting for the light-coupling mask, but a different background. In Fig. 6e, an additional layer is introduced in the background (i.e. in the Green tensor), serving as anti-reflection layer (bottom anti-reflection coating), as is often the case in lithography. Consequently, the standing wave in the photoresist caused by the reflections at the substrate interface (Fig. 6d) is completely suppressed (Fig. 6e). The numerical effort for both calculations is almost identical, although the physical systems are quite different.

In Eq. (20), the tensors **M** and **L** are used to handle the singularity of the Green tensor [90]. In particular, the tensor **L** represents the depolarization of the discretized volume [103]. There exists a completely different approach to the discretization of Eq. (19), where the singular terms **M** and **L** are skipped and another value is used for the dielectric contrast. As a matter of fact, $\Delta\varepsilon(\mathbf{r})$ is similar to the dielectric susceptibility $\chi(\mathbf{r})$, which in turn can be associated with the polarizability $\alpha(\mathbf{r})$ of the scatterer [104]. In the so-called DDA, also sometimes called the coupled dipole approximation, the polarizability of the scatterer is used in Eq. (20) instead of $\Delta\varepsilon(\mathbf{r})$ and the singular terms are omitted [91,105]. To obtain accurate results, the discretization takes into account the fact that the scatterer is decomposed into a lattice of dipoles and the polarizatbility of each mesh is obtained from the lattice dispersion relation instead of the scatterer's material properties [106].

The DDA usually considers a homogeneous background, where the Green tensor has the following additional symmetry property: $\underline{\underline{G}}^{\mathrm{b}}(\mathbf{r},\mathbf{r}') = \underline{\underline{G}}^{\mathrm{b}}(\mathbf{r}-\mathbf{r}')$. This translation property is easily understood with Fig. 6a: the field radiated at position $\mathbf{r}$ by a dipole located at position $\mathbf{r}'$ only depends on the relative distance $\mathbf{r}-\mathbf{r}'$ between both points; note that this property does not hold in the case of a stratified background, where the distances between these points and the interfaces also play a role (Fig. 6b). For a homogeneous background, Eq. (19) can be rewritten as

$$\mathbf{E}(\mathbf{r}) = \mathbf{E}^0(\mathbf{r}) + \int_{\mathrm{V}} \mathrm{d}\mathbf{r}' \underline{\underline{G}}^{\mathrm{b}}(\mathbf{r}-\mathbf{r}') \cdot k_0^2 \Delta\varepsilon(\mathbf{r}')\mathbf{E}(\mathbf{r}'), \quad (21)$$

which represents a convolution between the Green tensor and the source. Such a convolution can be easily computed in Fourier space, especially when the scatterer is discretized over a regular mesh and fast Fourier transform algorithms can be used [107]. This has led to an extremely efficient implementation of the DDA that uses fast Fourier transforms to speed up the integration [108]. A definite appeal of the DDA is that a very solid implementation of the technique is freely available [109].

The VIE method and DDA can be extended to periodic systems [110–112]. In this case, the periodic boundary conditions are handled by a specific Green function for which efficient acceleration techniques have been developed for its computation [113]. Let us finally mention that Eq. (19) forms the basis for a very general approximation for light scattering, namely the Born approximation. This approximation consists of using the illumination field $\mathbf{E}^0(\mathbf{r})$ instead of the unknown field $\mathbf{E}(\mathbf{r}')$, thus transforming the implicit Eq. (19) into an explicit equation, with the unknown electric field only on the left-hand side [114]. The procedure can be iterated, using the result of this first step as illumination field in Eq. (19) and so on. From a physical point of view, the first term in this Born series corresponds to the response of the different meshes in the system to the excitation, the second term to the first interaction between the meshes, and so on. In principle, this procedure should converge to the self-consistent solution of Eq. (19); unfortunately, the convergence is rather poor, especially for highly scattering materials, as encountered in nanophotonics [115]. This Born series has, however, inspired an iterative algorithm for the solution of Eq. (19) [116].

2.5. Surface integral methods

Surface integral methods reduce the computation of an electromagnetic scattering problem with open boundary conditions to the surface boundaries of materials. They work therefore best for piecewise homogeneous media. Two methods are used extensively in nanophotonics, namely the SIE method [26,117,118] and the boundary element method (BEM) [119]. We discuss first the SIE method, followed by the BEM and distinguish them by their usual implementation in nanophotonics.

The computational space is divided into domains V_n of relative permittivity ε_n and relative permeability μ_n. From Eq. (9), the electric field $\mathbf{E}$ in each region must satisfy the equation

$$\nabla \times \nabla \times \mathbf{E}(\mathbf{r}) - k_n^2 \mathbf{E}(\mathbf{r}) = i\omega\mu_n \mathbf{j}(\mathbf{r}), \quad \mathbf{r} \in V_n, \quad (22)$$

where $k_n^2 = \omega^2 \varepsilon_n \mu_n$ is the wavenumber for electromagnetic waves in region V_n and $\mathbf{j}$ denotes the volume current density. A dyadic Green function $\underline{\underline{G}}_n$ for region V_n is introduced:

$$\nabla \times \nabla \times \underline{\underline{G}}_n(\mathbf{r},\mathbf{r}') - k_n^2 \underline{\underline{G}}_n(\mathbf{r},\mathbf{r}') = \underline{\underline{1}}\delta(\mathbf{r}-\mathbf{r}'). \quad (23)$$

The equivalent surface current densities $\mathbf{J}_n = \hat{\mathbf{n}}_n \times \mathbf{H}$ and $\mathbf{M}_n = -\hat{\mathbf{n}}_n \times \mathbf{E}$ defined on the boundaries ∂V_n of the domains are introduced. Using Green's theorem, the electric field integral equation (EFIE) and the magnetic field integral equation (MFIE) can be derived on the domain boundaries [117]. A technique for solving the EFIE and the MFIE is the method of moments (MoM) [120]. The equivalent surface currents can be expanded in terms of Rao–Wilton–Glisson (RWG) basis functions $\mathbf{f}_i^n$ building a triangular mesh approximating the boundary surface ∂V_n [121]:

$$\mathbf{J}_n = \sum_i \alpha_i \, \mathbf{f}_i^n \quad (24)$$

$$\mathbf{M}_n = \sum_i \beta_i \, \mathbf{f}_i^n, \quad (25)$$

where the index i labels the different edges within all regions (Fig. 2e). If two RWG functions $\mathbf{f}_i^n$ and $\mathbf{f}_i^{n'}$ are associated with the same edge, the conservation of current on $\partial V_n = \partial V_{n'}$ between the two adjacent regions V_n and $V_{n'}$ implies $\mathbf{f}_i^n = -\mathbf{f}_i^{n'}$. If more than two regions are touching an edge, all the expansion coefficients related to this edge are identified. In this case, more than one RWG function is associated with the same edge, but only one per adjacent region. If the region V_n is not adjacent to the edge i, then

$\mathbf{f}_i^n \equiv 0$. The Galerkin method is applied, multiplying the EFIE and the MFIE with the basis functions and integrating over ∂V_n. Defining the sets $\{\alpha\}$ and $\{\beta\}$ of expansion coefficients α_i and β_i, the EFIE can be written as a matrix equation for $\{\alpha\}$ and $\{\beta\}$ for all regions:

$$\left[\sum_n i\omega\mu_n\mathbf{D}^n \quad \sum_n \mathbf{K}^n\right]\cdot\begin{bmatrix}\{\alpha\}\\ \{\beta\}\end{bmatrix} = \sum_n \mathbf{q}^{(E),n}, \qquad (26)$$

with sub-matrices

$$D_{ij}^n = \int\limits_{\partial V_n} \mathrm{d}S\, \mathbf{f}_i^n(\mathbf{r}) \cdot \int\limits_{\partial V_n} \mathrm{d}S'\, \underline{\underline{G}}_n(\mathbf{r},\mathbf{r}') \cdot \mathbf{f}_j^n(\mathbf{r}'), \qquad (27)$$

$$K_{ij}^n = \int\limits_{\partial V_n} \mathrm{d}S\, \mathbf{f}_i^n(\mathbf{r}) \cdot \int\limits_{\partial V_n} \mathrm{d}S' \left[\nabla' \times \underline{\underline{G}}_n(\mathbf{r},\mathbf{r}')\right] \cdot \mathbf{f}_j^n(\mathbf{r}'), \qquad (28)$$

and

$$q_i^{(E),n} = \int\limits_{\partial V_n} \mathrm{d}S\, \mathbf{f}_i^n(\mathbf{r}) \cdot \mathbf{E}_n^{\mathrm{inc}}(\mathbf{r}). \qquad (29)$$

In some cases, solving for $\{\alpha\}$ and $\{\beta\}$ with the EFIE or the MFIE does not result in the same values and can lead to large errors. Several combinations of SIEs can be considered, with different accuracy and convergence properties [122, 123]. The Poggio–Miller–Chang–Harrington–Wu–Tsai (PMCHWT) formulation combines EFIE and MFIE to solve them simultaneously [124]. Although the PMCHWT formulation might lead to poor conditioning of the system matrix and a slow convergence of iterative solvers [125], it has proven to give stable and accurate results [126, 127], even in resonant conditions [117]. In that case, the EFIE and the MFIE are combined:

$$\begin{bmatrix}\sum_n i\omega\mu_n\mathbf{D}^n & \sum_n \mathbf{K}^n \\ \sum_n \mathbf{K}^n & -\sum_n i\omega\varepsilon_n\mathbf{D}^n\end{bmatrix}\cdot\begin{bmatrix}\{\alpha\}\\ \{\beta\}\end{bmatrix} = \sum_n \begin{bmatrix}\mathbf{q}^{(E),n}\\ \mathbf{q}^{(H),n}\end{bmatrix}, \qquad (30)$$

with

$$q_i^{(H),n} = -\int\limits_{\partial V_n} \mathrm{d}S\, \mathbf{f}_i^n(\mathbf{r}) \cdot \mathbf{H}_n^{\mathrm{inc}}(\mathbf{r}). \qquad (31)$$

There are several ways to solve Eq. (30), among which are Gaussian elimination, LU factorization, and iterative methods. Overall, the number of numerical operations scales approximately with the sixth power of the particle size when Gaussian elimination is used, and can be brought to the fourth power with the conjugate gradient method [21]. The memory consumption scales approximately with the sixth power of the particle size. Once Eq. (30) has been solved on the domain boundaries, the electric and magnetic fields can be directly calculated at all points in space.

As a frequency-domain method, the SIE method can directly handle dispersive materials (similarly to the FE and VIE methods discussed previously). The matrix elements of Eq. (27) can be turned into integrals involving the scalar Green function $G_n(\mathbf{r},\mathbf{r}')$ or its gradient in their integrand, which is known to be divergent for $|\mathbf{r}' - \mathbf{r}| \to 0$. This behavior of the Green function can also lead to inaccurate results in the numerical evaluation of the matrix elements relative to neighboring triangles. An elegant way to overcome this difficulty is to separate the Green function into a singular part that can be integrated in a closed form and a smooth, slowly varying part that can be accurately integrated numerically. Highly conductive metals with Green function approaching a Dirac distribution can therefore be handled accurately. The same procedure can be repeated when evaluating the electric and magnetic fields, which guarantees an accurate field evaluation close to the scatterer surface. Similarly to the VIE method and as opposed to differential methods, the scattering, absorption, and extinction cross sections can be directly obtained without the use of absorbing boundary conditions. The discretization in elements allows for a great flexibility in rendering complex shapes, such as the defects that can arise in nanofabrication and their effect on optical properties. The SIE method was used in particular to investigate the near field and far field of realistic nanoantennas and compared them to that of idealized geometries [128]. Although their far field is comparable, the location of hot spots of the electromagnetic near field in the respective structures markedly varies, following the local variations of the shape. This has a strong influence on SERS or fluorescence signals [128, 129].

The SIE method can be generalized to multilayered plasmonic systems [130]. The Green function of homogeneous media (Eq. (23)) is replaced by the Green function of a layered medium Green function. Although the computation of this specific Green function is intensive, the discretization and the resulting system of equations are reduced to the nanostructured scatterers only. Compared to the VIE method, additional complications arise in the implementation due to the need to compute the curl of the Green function. In Ref. [130], this approach is used to study the spontaneous emission in complex multilayered plasmonic systems. Similarly to the VIE method, the SIE method can be generalized to periodic structures [113, 131, 132]. Reflection, transmission, and absorption are examples of measurable quantities that can be delivered, in addition to phase information of the field as well as orders of diffraction. An example of implementation to a complex resonator supporting Fano-like plasmonic resonances is shown in Fig. 7. The ability to monitor simultaneously the near field and the far field of the SIE method has revealed their relation [133, 134]. In particular, it has been observed that the maximum in field enhancement does not correspond to particular features of the far field (neither a local maximum nor minimum) but is determined by the condition of Fano interference. Quantitative information on the field enhancement is also obtained with the SIE method: in this case, the intensity of the near field at the resonance

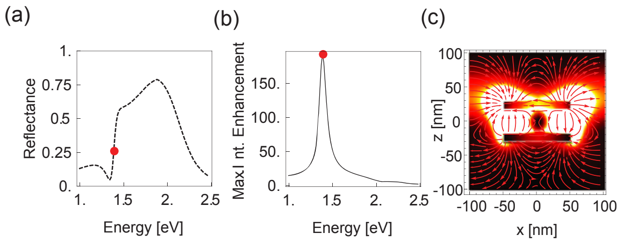

Figure 7 Fano resonance in a periodic system of strongly coupled gold nanowires. (a) Reflectance spectrum for top illumination. (b) Maximum intensity enhancement sampled at a distance of 1 nm around the surface. (c) Normalized electric field intensity enhancement with field lines. Adapted from Ref. [133] with permission. Copyright (2011) Optical Society of America.

wavelength increases to 200 times the intensity of the incident field.

Other formulations such as the electric and magnetic current combined field integral equation (JMCFIE) also involve SIEs with the normal components of the fields [118,123]. A comparative study by Araújo *et al.* of the cross sections of nanoparticles in silver, gold, and aluminum of various sizes has shown in particular that the PMCHWT formulation is more accurate than the JMCFIE formulation [122]. However in these cases, JMCFIE shows a better convergence for iterative solvers, which makes it more suited for large systems than PMCHWT. The JMCFIE formulation has been combined with the multilevel fast multiple algorithm (MLFMA) which enables the computation of large plasmonic systems, with characteristic dimensions up to several wavelengths [135]. This approach has been in particular recently applied to the simulation of SERS enhancement in a variety of large nanophotonic systems, such as highly complex disordered stacks of gold nanorods or three-dimensional photonic crystals [136]. In Fig. 8, a large amount of nanoparticles are dispersed randomly. The multiple plasmon couplings with random local arrangements and mode shifts induce a significant spectral broadening. The hot spots and their evolution as a function of the frequency can be studied in detail, which is useful in particular for sensing or SERS. Other approaches for the computation of large systems using integral methods have been more recently developed, such as the adaptive cross approximation [137] or the broadband MLFMA [138], which can handle features small compared to the wavelength.

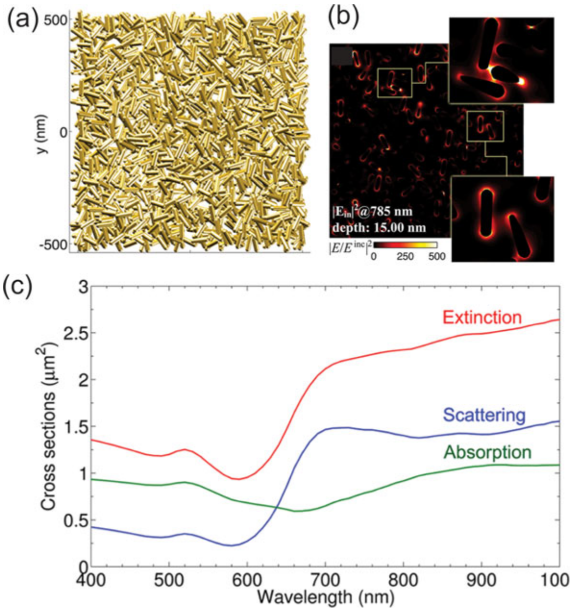

Figure 8 Far-field and near-field properties of highly complex disordered plasmonic structures computed with the SIE–JMCFIE method accelerated with the MLFMA algorithm. (a) Top view of an in-water colloidal deposition of 1447 gold nanorods (size 80 × 21 nm^2) with a minimum separation distance of 1 nm. (b) Electric field intensity enhancement map. (c) Scattering, absorption, and extinction cross sections. Adapted from Ref. [136] with permission. Copyright (2014) American Chemical Society.

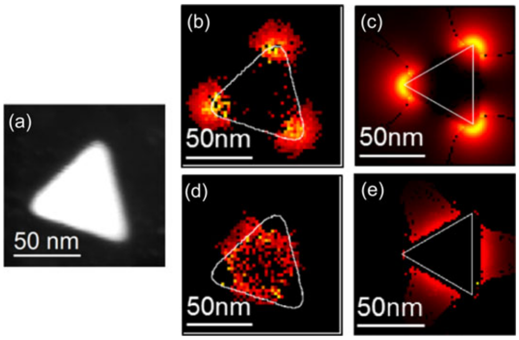

Figure 9 EELS maps of individual nanoprisms measured experimentally and compared to BEM calculations. (a) High-angle annular dark field image of a nanoprism. (b) Experimental EELS map of a dipolar mode. (c) Corresponding BEM calculation. (d) Experimental EELS map of a higher order mode. (e) Corresponding BEM calculation. Adapted from Ref. [49] with permission. Copyright (2015) American Chemical Society.

As compared to SIE, the BEM introduced to nanophotonics by Aizpurua *et al.* uses the Green function to compute the scalar and vector potentials at surface boundaries [139]. The discretization of the surface integrals is performed over a set of points, contrary to the use of elements and basis functions for SIE. The BEM is therefore in essence easier to implement than SIE but on the other hand is also more limited in the computation of plasmonic systems with large field gradients and fine geometrical variations. It has proven to be highly efficient in computing the optical properties of nanoparticles such as produced by chemical synthesis [23, 140]. In a recent experiment, the BEM was used to correlate EELS and cathodoluminescence signals with optical scattering and extinction, respectively [49]. As can be seen in Fig. 9, a good agreement between the EELS maps of gold nanoprisms and BEM calculations is observed. In particular, the existence of two modes of different orders is revealed. The near field calculated in the BEM can also be used for particular applications such as optical heating [141]. A robust implementation of the BEM in Matlab is freely available [142].

Table 1 Summary of methods and nanophotonic problems: xxx, very good match; xx, good match; x, can be adapted.

Method	Propagation	Localization	Scattering
Finite differences in time domain	xxx	x	x
Finite elements	xx	xxx	x
Discontinuous Galerkin in time domain	xxx	xx	x
Volume integral equations	x	x	xxx
Surface integral equations	x	xx	xxx
Rigorous coupled wave analysis	x	x	xx

2.6. Other methods

This section covers other approaches for solving Maxwell's equations than the differential and integral methods. First, the hybrid differential–integral methods are particularly efficient in solving certain problems such as anisotropic or inhomogeneous scatterers [63]. The finite integration technique (FIT) is a discretization scheme for Maxwell's equations in their integral form [65]. In contrast to differential and integral methods which can cover a broad range of systems, some other methods are known to be very efficient for specific conditions and geometries as they rely on expansions of the electromagnetic field on basis functions that have a particular symmetry. In the T-matrix method, the incident and scattered electromagnetic fields are expanded on a set of spherical basis functions, with boundary conditions enforced at interfaces between the different materials. This method is particularly efficient for calculating the scattering of spherical or quasi-spherical particles or aggregates [143]. It has been extended to layered particles and particles interacting with substrates, and applied to plasmonics, with applications in particular for sensing, SERS, and plasmonic trapping [144, 145]. The multiple multipole program, also known as the generalized multipole technique, is a semi-analytical method that expands the electromagnetic field in multipoles which allows it to tackle a broad variety of geometries [146, 147], including plasmonic nanostructures [25]. With this approach, only the boundaries of the domains have to be discretized and no integrals have to be solved numerically. For clusters of nanoparticles, the multiple elastic scattering of the multipole expansions decomposes the scattered fields into multipoles with respect to centers close to each of the objects of the cluster and multiple scattering is carried out until convergence is achieved [141, 148].

The RCWA applies the diffraction of electromagnetic waves by periodic grating structures. The periodic permittivity and the electromagnetic field are expanded in Fourier series and boundary conditions are enforced at material boundaries [149]. This results in a rather poor rendering of abrupt surfaces which require a high number of Fourier harmonics. The method is very efficient for the calculation of far-field reflection and transmission coefficients, as well as diffraction orders, but the accurate computation of the near field at material boundaries remains challenging [150]. It had originally a limited accuracy for the TM polarization, which was later improved [28, 151, 152]. Examples of implementation of the RCWA include anti-reflection coatings for solar cells [28] and plasmonics [153]. The Chandezon method (or C-method) is a popular stable method for the simulation of diffraction gratings [154] which can also be applied to plasmonics [151]. Methods based on transformation optics use the solution of a simple system, which can be solved analytically, and use coordinate transformations to find the solution of a more complex system [155, 156].

2.7. Summary

Numerical methods for solving Maxwell's equations together with linear constitutive relations for the electric and magnetic fields have been reviewed. Their applications to typical problems in nanophotonics have been discussed based on their fundamental equations and recent examples from the literature. We base our discussion on the categories of fundamental nanophotonics problems identified and defined in Section 1.2: problems related to light propagation, localization, and scattering. Problems requiring modeling beyond Maxwell's equations are discussed in Section 3.

Table 1 recapitulates the discussion of this section by evaluating the match between problems and methods. There exist a manifold of different methods, but the methods in Table 1 have been selected as particularly representative for certain categories. Other methods that are similar in their fundamental equations would also have similar efficiency in solving the corresponding problems. We now comment on how the points were attributed in Table 1. Methods in the time domain such as FDTD and DGTD can deliver explicit information of light propagation in waveguides (or more generally systems confining light in one or two dimensions) such as decay lengths in lossy waveguides, and are therefore most suited for problems based on light propagation. This is a challenging task for frequency-domain methods. On the other hand, the FE method can give access to mode frequencies in waveguides. Problems involving light localization involve resonant effects and usually require knowledge of the near field and spectral properties. The DGTD method, as an accurate time-domain method, partially satisfies these requirements. Frequency-based methods are better suited, with the exception of VIE methods (as defined in this review) which have limited accuracy in evaluating the near field. In general, integral methods are also limited to smaller systems as the FE method. For light scattering, integral methods are the preferred choice. SIE can handle larger systems than VIE but is also limited to piecewise homogeneous scatterers. RCWA has in comparison less flexibility in geometries, although it is particularly efficient for periodic systems.

In general, it has been shown that there always exists one or several methods that are particularly suited for a given category of problems. In these cases, the structure of the fundamental equations of the methods shows that they are able to directly and efficiently provide a solution. In most cases when the match between the method and the systems is not optimal, the method can still provide a solution but an additional development or computational effort may be required. The modeling of nanophotonic systems should involve finding the solution of one or several problems included in these categories. The reader is invited to consider the ranking of the associated columns in order to make a choice of method: for example, in the case of a quantum dot with a nanoantenna (such as in Ref. [48]), the coupling from the quantum dot to the near field as well as the radiation pattern of the nanoantenna are important for the emission efficiency. In such cases, the input from the localization and scattering columns should be considered together and SIE methods appear to be the most efficient. In another example, if the quantum dot is coupled to a waveguide, the FE and DGTD methods are the most appropriate by considering inputs from the propagation and localization columns.

3. Next modeling challenges in nanophotonics

In this section, we review the different numerical techniques for nonlinear and quantum nanophotonics and the upcoming challenges related to these recent topics. Nonlinear and quantum effects play an important part in the development of modern optics in general and in nanophotonics in particular. Furthermore, a multitude of nonlinear optical processes can be observed in nanostructures. The aim of the present section is not to provide a complete overview of nonlinear optical processes, but to present some of their particularities in relation to suitable numerical treatments (Section 3.1). In Section 3.2, active systems requiring optical and electronic simulations are discussed. The recent advances in nanofabrication have revealed that the predictions from classical electromagnetism fail for tiny nanostructures and narrow gaps, and the development of new numerical approaches including nonlocal dielectric functions (Section 3.3) or quantum effects (Section 3.4) is mandatory in order to provide accurate evaluation of their optical properties. Finally, the specific and important case of graphene nanostructures is addressed (Section 3.5).

3.1. Nonlinear optical processes

The observation of nonlinear optical processes requires high pump intensity. Interestingly, the localization of light in nanovolume increases the local field intensity making the observation of nonlinear optical processes possible at the nanoscale [51]. Various nonlinear optical processes are observable in nanophotonics depending on the matter properties and the excitation conditions (Fig. 10a) [51]. Obviously, it is important to classify them in order to develop systematic approaches for their numerical evaluations. The first necessary distinction is between parametric and nonparametric optical processes. Boyd writes is his textbook about nonlinear optics [157]: “The origin of this terminology is obscure but the word parametric has come to denote a process in which the initial and final quantum-mechanical states of the system are identical.” And “A difference is that photon energy is always conserved in a parametric process; photon energy need not be conserved in a nonparametric process, because energy can be transferred to or from the material medium.” In other words, there is no transfer of energy, momentum, or angular momentum between the nonlinear medium and the electromagnetic wave during a parametric optical process.

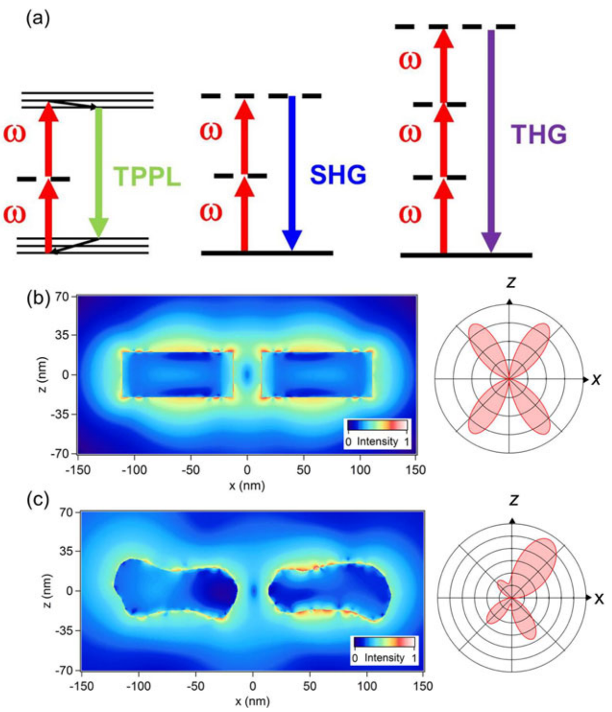

Figure 10 (a) Jablonski diagrams describing TPPL, SHG, and THG. Near-field distributions of the second harmonic intensity and the corresponding nonlinear emission patterns computed for (b) an idealized nanoantenna with rectangular arms and (c) a realistic nanoantenna described by a mesh adapted from a scanning electron microscope image. Adapted with permission from Ref. [176]. Copyright (2013) American Chemical Society.

Before discussing the parametric processes in greater detail, it is worth saying a few words about an important nonparametric nonlinear optical process, namely two-photon photoluminescence (TPPL), mainly because this process has been widely studied and observed in gold nanostructures [158–160]. TPPL is a three-step process involving the excitation of an electron–hole pair by the absorption of two incident photons, the relaxation of the excited electrons and holes, and the emission of light due to the recombination of electron with hole. TPPL results in a broadband signal. The TPPL intensity for an emission frequency ω_2 resulting from a pumping beam with a frequency ω_1 is given by[161]

$$I(\omega_2) = \eta(\omega_2)|E_0|^4|L^4(\omega_1)L^2(\omega_2)|, \tag{32}$$

where ω_1 and ω_2 are the incident light and TPPL frequencies, respectively, and η is a factor related to the intrinsic luminescence spectrum of the material. The local field factors $L(\omega)$ at the excitation and emission frequencies are related to the electric field enhancement close to the considered nanostructure [161]. More specifically, the local field factors are defined as the ratio between the local electric field and the incident electric field. The computation of the electric field enhancement can be performed using one of the numerical methods discussed in this review. The evaluation of the parameter η is more complicated and requires considering the band structure of the studied material [158]. However, this evaluation is not mandatory for understanding the trend of the influence of plasmon resonance on TPPL and for designing efficient plasmonic nanostructures with high TPPL for specific applications [162].

Let us now turn our attention to parametric processes. Such nonlinear effects are described by re-writing the polarization as [157]

$$\mathbf{P}(t) = \varepsilon_0(\chi^{(1)}\mathbf{E}(t) + \chi^{(2)}\mathbf{E}^2(t) + \chi^{(3)}\mathbf{E}^3(t) + \cdots). \tag{33}$$

The quantities $\chi^{(2)}$ and $\chi^{(3)}$ are the second- and third-order nonlinear susceptibilities, describing, respectively, the second- and third-order nonlinear optical processes. The second- and third-order nonlinear susceptibilities are responsible for different nonlinear optical processes. For example, the second-order nonlinear susceptibility is responsible for SHG, the process whereby two photons at the fundamental frequency are converted into one at the second harmonic (SH) frequency. The third-order nonlinear susceptibility is responsible for THG, the process thereby three photons at the fundamental frequency are converted into one at the third harmonic (TH) frequency [157]. The properties of nonlinear susceptibilities are directly related to the properties of the nonlinear medium and closely related to the symmetry selection rules. For example, it is well known that SHG (a second-order nonlinear optical process) is forbidden in centrosymmetric media in the electric dipole approximation, which explains its surface sensitivity [163, 164]. Numerical methods based on FE methods [165–167], BEM [123, 168, 169], hydrodynamic models [170–173], FDTD [174], VIE [175], and SIE methods [176–178] have been developed for the computation of SHG from plasmonic nanosystems. The frequency conversion in nanostructures is relatively weak meaning that the undepleted pump approximation is valid and that the computation of the nonlinear signal can be decomposed into three distinct steps: evaluation of the fundamental near-field intensity/electric field, evaluation of the nonlinear sources, i.e. the nonlinear polarization, and evaluation of the nonlinear electromagnetic field.

The main challenge for accurate computation of the surface SHG is the correct evaluation of the fundamental electric field very close to the boundary surface. For doing so, BEM and SIE have been shown to be methods of choice since the electric field close to the interface can be evaluated directly from the surface current. Furthermore, numerical methods requiring the discretization of the boundary surfaces only are more suitable for surface SHG, reducing the computation time and the necessary memory [168, 177]. In contrast, THG is not forbidden in a centrosymmetric medium and the TH intensity is expected to arise from the volume of the nanostructures [179]. In this case, a volume discretization is required for a convenient evaluation of the TH signal and the use of FE or volume integral methods seems to be more appropriate [180–183]. Even though SIE can, in principle, be used to model THG, the expression of the nonlinear sources taking place in the nanoparticle volume in terms of surface unknowns is not straightforward. The symmetry properties of SHG not only influence the origin of the SH signal but also strongly affect the influence of the nanostructure shape on the SH scattered wave [165]. Indeed, the SH signal is strongly modified by any deviation from perfectly symmetric shapes. This point is very important for nonlinear nanophotonics and plasmonics opening the possibility of nonlinear ultrasensitive optical characterization[176]. Indeed, despite the recent progress in nanofabrication, it is not possible to realize perfect nanostructures and small defects, such as surface roughness for example, are always observed. Computations using a SIE approach have demonstrated that the SHG from a realistic nanoantenna differs from that from an idealized one although both nanoantennas have an identical linear response (Fig. 10b,c) [176]. As a consequence, depending on the expected degree of accuracy required for describing experimental results, it is necessary to use a mesh describing accurately the real shape of the fabricated samples.

Although the numerical modeling of nonlinear optical processes in nanosystems is nowadays well established, there are still open questions and a higher level of refinement is still possible. For example, the relative role of the conduction and core electrons in the nonlinear response has not been unambiguously determined. Indeed, it was shown that the electronic transitions with initial and intermediate states standing in the d-band contribute significantly to the SHG from a gold surface [184], while the hydrodynamic model only considers the influence of the core electron on the motion of the conduction electrons [185]. So far, the crystallinity of nanoparticles has been neglected in the numerical modeling of nonlinear effects but it can play an important role, even for surface response, due to the tensorial nature of the nonlinear response [157].

3.2. Active systems

Some nanophotonics systems such as gain media in amplifiers and lasers require a modeling of electron populations with multilevel quantum systems in addition to the electromagnetic field. The constitutive equations for the electric field are not linear. In a semi-classical approach, the equations of a multiple level quantum system can be solved numerically in the time domain, simultaneously with the equations for the electromagnetic field [56, 186]. Recent examples of such a problem solved by FDTD with auxiliary differential equations are shown in Ref. [187] where the output emission intensity of a nanolaser built from a strongly coupled plasmonic nanoparticle array is computed as a function of the input pump pulse energy, or in Ref. [188] for modeling metamaterials with gain. As nonlinear terms are involved in the rate equations coupled to Maxwell's equations, time-domain methods (such as FDTD, FETD, and DGTD) are more appropriate than frequency-domain methods.

In light harvesting systems such as solar cells [38, 39], various light management strategies have been implemented in order to increase the absorption in the active layer. Modeling of the efficiency of such complex systems requires state-of-the-art optical simulations in addition to the transport physics. In Ref. [189], coherent simulations of light propagation in a thin-film silicon solar cell have been performed to study the influence of interface patterning on the photocurrent. Various light management scenarios involve nanoscale patterning of the active layer or even the introduction of plasmonic nanostructures to enhance light absorption by near-field effects [38, 39]. A complete understanding of their influence on the efficiency would require modeling of the electronic properties in such complex systems with nanopatterned interfaces.

3.3. Nonlocal effects

A nonlocal correction of the linear Maxwell's equations is required for particles of small size, which implies challenges in the computation of their optical properties. An important parameter for the description of the material properties is the dielectric constant. In the local approximation, the electric displacement at a given point is a function of the electric field at this given point and $\mathbf{D}(\mathbf{r}, \omega) = \varepsilon(\omega)\mathbf{E}(\mathbf{r}, \omega)$, where $\varepsilon(\omega)$ is the local permittivity at the frequency ω. This dispersive local permittivity can be either interpolated from experimental results or theoretically evaluated. However, the local bulk permittivities fail to accurately describe the optical responses of small plasmonic nanoparticles. If the nanoparticle diameter is reduced below ~ 10 nm, then the nanoparticle size is comparable to the mean free path of the conduction electrons increasing the electron scattering rate at the nanoparticle surface. In order to describe this effect, the dielectric function of a metal can be phenomenologically rewritten as [190]

$$\varepsilon(\omega) = \varepsilon^{\mathrm{loc}}(\omega) + \frac{\omega_{\mathrm{p}}^2}{\omega(\omega + i\eta)} - \frac{\omega_{\mathrm{p}}^2}{\omega(\omega + i\eta + iv_{\mathrm{F}}/a)}, \tag{34}$$

where $\varepsilon^{\mathrm{loc}}(\omega)$ is the local part of the response which can be taken from optical measurements [191], ω_{p} is the electron gas plasma frequency, η is the width of the metal bulk plasmon, v_{F} is the Fermi velocity, and a is the nanoparticle radius. The size-corrected dielectric function leads to satisfactory values for both plasmon energy and width (Fig. 11a) [192]. In comparison with the bulk permittivity, the corrected dielectric function results in a broadening of the surface plasmon resonances supported by small spherical nanoparticles due to additional energy dissipation. Note that the size-corrected dielectric function does not reproduce the surface plasmon resonance blueshift induced by nonlocal effects. Furthermore, such a phenomenological modification of the dielectric constant is possible only in the case of compact metallic nanospheres but is difficult to apply for nonspherical nanoparticles [193, 194]: even the description of plasmonic nanoshells is not straightforward since the electron scattering rate depends on both the core radius and the shell thickness [195].

In a more general way, the electric displacement in a nonlocal medium must be written as

$$\mathbf{D}(\mathbf{r}, \omega) = \int \mathrm{d}\mathbf{r}'\varepsilon(\mathbf{r}, \mathbf{r}', \omega)\mathbf{E}(\mathbf{r}, \omega), \tag{35}$$

where $\varepsilon(\mathbf{r}, \mathbf{r}', \omega)$ is the nonlocal dielectric function. This expression is said to be "nonlocal" because the dielectric function at one given point of the nanostructure depends on the electric field at other points. Analytical expressions have been developed for describing the important case of the free electron gas. It has been proposed to model the dielectric constants of metals by subtracting the Drude part ε^{D} from the measured permittivity $\varepsilon^{\mathrm{loc}}$ and then adding the Mermin dielectric function ε^{M} [196]:

$$\varepsilon(\mathbf{q}, \omega) = \varepsilon^{\mathrm{loc}}(\omega) + \varepsilon^{\mathrm{M}}(\mathbf{q}, \omega) - \varepsilon^{\mathrm{D}}(\omega), \tag{36}$$

where $\mathbf{q}$ is the momentum. In the specular reflection model [197, 198], the response of a nanostructure is expressed in terms of the nonlocal dielectric function of the bulk material and the continuity of the potential and the electric displacement are imposed at the interface assuming that each medium is infinitely extended. Auxiliary boundary charges are defined on each side of the interface to guarantee these boundary conditions. The specular reflection model has a good agreement with experimental results (Fig. 11a) [198]. However, this approach is still restricted to simple geometries including spherical nanoparticles due to the required computation memory. Note that the nonlocal optical properties of nanoshells and nanodimers can be evaluated with this approach [199]. As observed in the case of compact nanospheres, the nonlocal effects result in a blueshift of the surface plasmon resonances supported by gold nanodimers (Fig. 11b) [199].

Recently, numerical schemes combining a hydrodynamic description of the conduction electron response with FE or FDTD methods have been proposed [200–202]. The nonlocal calculations require more computation memory than local ones. Indeed, the numerical grid size has to be

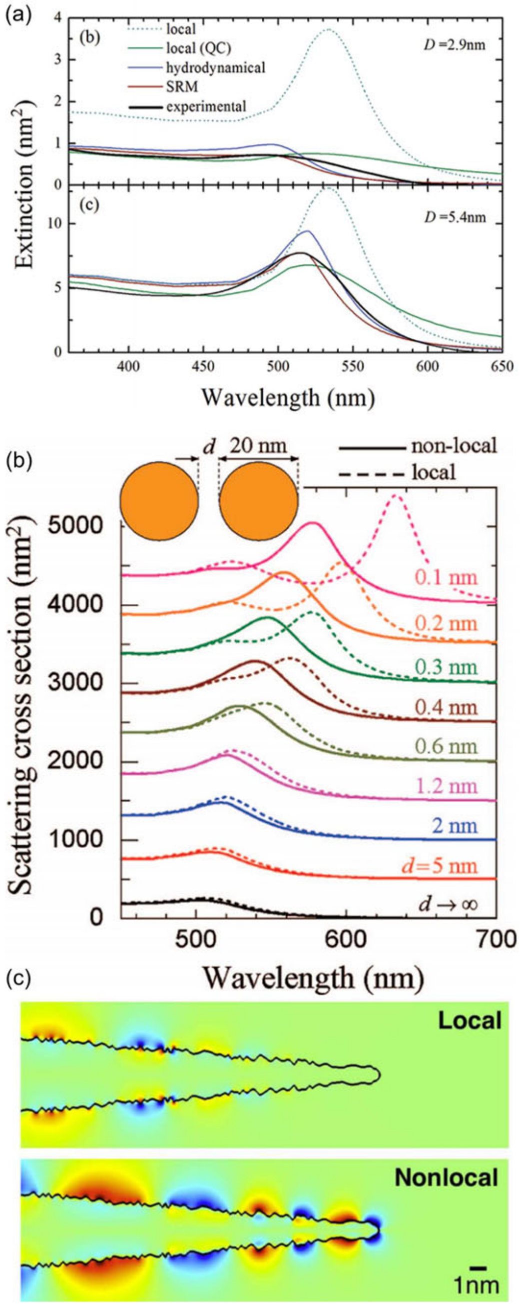

Figure 11 (a) Extinction cross section as a function of incident wavelength evaluated with various numerical approaches. The sphere diameter is $D = 2.9$ nm (top panel) and $D = 5.4$ nm (bottom panel). Adapted with permission from Ref. [199]. Copyright (2011) American Chemical Society. (b) Comparison between the local and the nonlocal responses of gold nanodimers with various gap dimensions. Adapted with permission from Ref. [198]. Copyright (2008) American Chemical Society. (c) Focusing properties of a silver nanotip computed with a local description (top panel) and a nonlocal description (bottom panel). Adapted with permission from Ref. [201]. Copyright (2012) American Chemical Society.

much smaller than the Fermi wavelength ($\lambda_F \sim 0.5$ nm for silver and gold) and not only smaller than the incident wavelength and the nanostructure size. Examples of the nonlocal response of complex plasmonic nanostructures, e.g. gold bowtie nanoantennas and a gold nanotip, have been reported (Fig. 11c) [200–202]. In the case of nanoparticle dimers and gold nanotips, the field enhancements predicted considering a nonlocal response are smaller than those obtained with a local description. Furthermore, spectral differences arise when nonlocality is addressed approximately, compared to a full quantum treatment of the dynamical screening [203]. This behavior is dramatic for most of the applications in plasmonics including SERS and nonlinear optics because the scattered intensity varies nonlinearly with the fundamental intensity for these optical processes [200–202]. The combination of a SIE method with the hydrodynamic Drude model has been proposed in order to reduce the required memory for the evaluation of nonlocal effects in plasmonic nanostructures [204]. In this case, an additional SIE is required for taking into account the longitudinal waves existing in the metal. This method has been used for describing nonlocal effects in infinite plasmonic nanowires standing on the top of a dielectric substrate [204]. A blueshift of surface plasmon resonances, which increases as the radius of the nanowire decreases, is also induced by the nonlocal effects. The same approach for three-dimensional nanostructures, where the advantages associated with a surface method are even more important, has to be developed taking into account the boundary conditions for the longitudinal waves. This will be particularly appealing in the case of realistic nanostructures modeled with SIE [128].

3.4. Quantum plasmonics

The phenomenological inclusion of nonlocal effects in various classical modeling approaches has been discussed in the previous section, showing a good agreement between theoretical predictions and experimental results. However, full quantum calculations are necessary for the accurate description of specific physical effects such as electron screening effects, spill-out, and tunneling [52]. In this context, time-dependent density functional theory (TDDFT) has been widely used for the computation of the optical and electronic properties of small metallic clusters [205–209]. The dynamics of the conduction electron fluid is described with a jellium model, for which the discrete ionic background is replaced by a continuous box with a constant potential reproducing the electron density in a real metal. Even though the TDDFT is a considerable simplification of the quantum description of the many-body problem, the number of involved conduction electrons, and then the dimension of the considered nanostructures, is still limited by computer memory [210, 211]. As a consequence, TDDFT has been only used to describe metallic nanostructures with simple geometries including objects with spherical symmetries, such as compact nanospheres [211] and nanoshells [212, 213], but also elongated objects such as Na wires

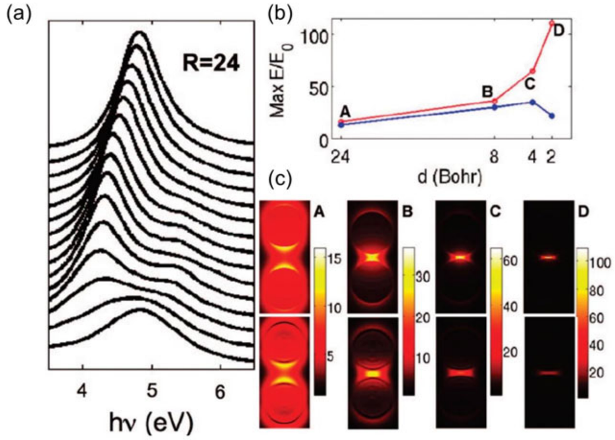

Figure 12 (a) TDLDA absorption spectrum for dimers of spheres (sphere radii $R = 24$ Bohr radius) and gap separation ranging from 0 to 24 Bohr radius. The nanosystem contains 1018 conduction electrons. (b) Maximum field enhancement in the nanogap for classical computation (red line) and TDDFT (blue line). (c) field enhancement close to the dimer for various gap dimensions. Classical computations are shown in the top panels and the results from TDDFT are shown in the bottom panels. Adapted with permission from Ref. [220]. Copyright (2009) American Chemical Society.

[192] and silver nanorods [214, 215] with different aspect ratios.

The quantum interaction between close nanostructures is even more complicated to compute [216–219]. The main physical effects that cannot be taken into account in classical modeling are the electron tunneling and the current occurring in very small gaps (below ~ 1 nm). Figure 12 shows the absorption and compares the field enhancement obtained for classical electromagnetic modeling and time-dependent local density approximation (TDLDA) for different separation distances [220]. For gaps ranging from 1 to 0.5 nm (the so-called crossover regime), the nanogap is characterized by an electron potential which can be tunneled by the conduction electrons making the quantum effects important in this regime. In this case, classical modeling approaches are not able to accurately describe the optical response due to the charge transfer between the nanoparticles. For even smaller nanogaps (< 0.5 nm), the conductive regime is reached and the conductance in the nanogap is high allowing the conduction electrons to flow between the nanoparticles and resulting in a new plasmonic mode called a charge transfer plasmon. The charge transfer plasmon blueshifts when the distance between the nanoparticles decreases.

Beyond these first-principles methods, a quantum corrected model (QCM) has been recently proposed for studying the quantum effects in the optical properties of large coupled plasmonic nanoparticles [217, 221]. In this model, a fictitious load is added between the nanoparticles in order to mimic the quantum electron tunneling. The permittivity of the load is evaluated with a quantum mechanical calculation of the electron transmission probability. Although the BEM was used in Ref. [217], the calculation of the optical response of plasmonic nanostructures in the QCM can be done with most of the numerical methods discussed in Section 2. However, FE method and VIE seem to be particularly well suited for this purpose since the permittivity of the fictitious load is a function of the position. The QCM is a powerful approach and will probably be the bridge between quantum plasmonics and nonlinear plasmonics in the near future [222, 223]. It will also be interesting to determine how the QCM can be extended to nanogaps with complex geometries [128, 224].

3.5. Graphene nanostructures

Graphene is a single two-dimensional layer of carbon atoms organized in a honeycomb lattice [225]. Graphene has recently emerged as an important material for the design of new nanophotonic elements [226–228]. Indeed, the unique electronic band structure of graphene results in interesting optical properties promising for the design of optical devices [229]. For an example, a single undoped graphene layer can absorb a quantity of light as high as 2.3%, which is promising for the development of compact optical detectors [230]. Close to the Fermi level, the specificity of the electronic band structure of graphene, is the existence of two singular points in the first Brillouin zone [229]. The injection of charge carriers opens up a gap of $2E_\mathrm{F}$, where the Fermi energy E_F is related to the carrier density. As a consequence of the Pauli blocking effects, photons with energy lower than $2E_\mathrm{F}$ are not absorbed in doped graphene. It was also demonstrated that highly doped graphene can support surface plasmon resonances. Interestingly, the plasmonic properties of graphene have the ability of being electrically tunable, underlying the flexibility of this material for nanophotonics [231, 232]. Tunable plasmon resonances have been reported in various graphene systems such as extended graphene [53], ribbons [233, 234], disks [232, 235], rings [236], graphene nanoantennas [237], and metasurfaces [238, 239].

The key point for determining the optical response of extended graphene and graphene nanostructures is the evaluation of the electrical conductivity $\sigma(k_\parallel, \omega)$, where $k_\parallel$ is the in-plane electron momentum. This has been done using the random phase approximation (RPA) using a tight-binding description of the π-band electron wave functions [240, 241]. In the limit of a collision rate of carriers small in comparison with the frequency and spatial dispersion of the AC electric field, the graphene conductivity reduces to [242, 243]

$$\sigma(\omega) = \frac{e^2\omega}{i\pi\hbar}\left[\int_{-\infty}^{+\infty} \mathrm{d}\varepsilon \frac{|\varepsilon|}{\omega^2}\frac{\mathrm{d}f_0(\varepsilon)}{\mathrm{d}\varepsilon} - \int_{-\infty}^{+\infty} \mathrm{d}\varepsilon \frac{f_0(-\varepsilon) - f_0(\varepsilon)}{(\omega + i\delta)^2 - 4\varepsilon^2}\right], \qquad (37)$$

where f_0 is the electron distribution which depends on both the Fermi energy E_F and the temperature T, e is the elementary electric charge, $\hbar$ is the reduced Planck constant, ε is the energy, and δ is the infinitesimal quantity determining the bypass around the integrand pole. The second term of this equation corresponds to the intraband transition, which results in the Drude conductivity at zero temperature:

$$\sigma^{\text{intra}}(\omega) = \frac{e^2}{\pi\hbar^2}\frac{iE_{\mathrm{F}}}{\omega + i\tau^{-1}}. \tag{38}$$

The second term corresponds to the interband transitions across the gap. When the collision rate τ^{-1} tends to 0, this term is easily computed as [242, 243]

$$\sigma^{\text{inter}}(\omega) = \frac{e^2}{4\hbar}\left[G\left(\frac{\omega}{2}\right) - \frac{4\omega}{i\pi}\int_0^{+\infty} \mathrm{d}\varepsilon \frac{G(\varepsilon) - G(\omega/2)}{\omega^2 - 4\varepsilon^2}\right], \tag{39}$$

where

$$G(\varepsilon) = \frac{\sinh(\varepsilon/T)}{\cosh(\mu/T) + \sinh(\varepsilon/T)}, \tag{40}$$

in which μ is the chemical potential. This formula gives reasonably accurate results for the analysis of graphene plasmons [231, 232]. The dielectric function of graphene is directly related to the conductivity by the formula $1 + 4\pi i\sigma/\omega t$. The electromagnetic response of nanostructured graphene has been computed implementing this dielectric function in the FE method [237] and the BEM [231, 232]. Figure 13 shows a comparison between first-principles calculations based on the RPA and classical computation. Note that the classical computation takes into account the quantum nature of the electronic response but the edges are treated in a classical way [237]. A good agreement is found for the classical computations and the RPA ones considering armchair (ac) edges but not for zigzag (zz) edges. This discrepancy is explained by the near-zero-energy electronic states observed in zz edges, which result in additional losses. The faster plasmon decay induces a lower field enhancement in graphene nanoantennas with zz edges [237].

The ultrafast transient response of graphene sheets has been recently investigated and the relative role of the intraband and interband transitions discussed [244, 245]. The ultrafast response of graphene nanostructures is of great importance for the design of high-speed and compact optical devices. To the best of our knowledge, numerical methods for evaluating the transient response of graphene nanostructures have not been reported in the literature yet. The direct introduction of the transient dielectric constant of graphene in classical modeling methods, as discussed previously in the continuous regime, is a rough approach but can probably be used as a first step for the understanding of experimental results.

4. Summary and outlook

Nanophotonics includes the science and engineering of light manipulation and confinement at the nanoscale. The modeling of nanophotonic systems has been decomposed into four categories of problems: those involving light propagation, light localization, light scattering, and multiscale systems. A broad variety of materials and geometries can be involved with a dynamic range of the electromagnetic field which can span several orders of magnitude, with the amplitude of the electric field going from zero to several hundreds over a few nanometers at the edge of a plasmonic nanostructure, for example. These characteristics make the accurate and efficient modeling of nanophotonic systems extremely challenging, but also of utmost importance for the analysis and the development of new components and devices.

A large portion of problems in nanophotonics can be currently modeled with classical Maxwell's equations. A diversity of methods have been developed and used for the modeling, understanding, and design of nanophotonic systems, shared between commercial and freeware implementations. Among them, two categories of versatile methods have been reviewed: differential (FDTD, FE, and hybrid FD/FE) and integral (VIE, SIE) methods . Other methods are specific to certain geometries but also very efficient (such as RCWA). Each method is based on a specific equation derived from classical Maxwell's equations, which determines the typical problems it can tackle. Therefore, there is no ultimate method for modeling nanophotonic systems as such and it is very important to have a basic understanding of the assumptions behind a given numerical method in order to use it at its best and obtain the most reliable results. This review was aimed at providing the reader with sufficient information to choose the most appropriate method for the problem at hand. References were provided, which point to detailed descriptions of the methods. The main conclusions of Section 2 are summarized in Table 1. In particular, methods in the time domain such as FDTD and DGTD have been identified as very well suited for problems involving light propagation. For problems based on light localization, the FE and SIE methods are particularly efficient. Finally, VIE- and SIE-based methods as well as RCWA are very well suited for problems involving light scattering.

Current and future developments tend to enlarge the scope of these methods, that is, adapt them to systems for which they were not originally designed. This can of course be an advantage for the user of a method if the capability can be extended without the requirements for investing in the implementation or purchase of another software. The simulation of larger systems or with higher accuracy calls for further developments and optimizations of both methods and solvers. Nanophotonic systems are also at the stage where they can be implemented and combined together in integrated devices. This requires a multilevel modeling where several methods are combined together to simulate the entire device. The engineering of nanophotonic devices also calls for the use of optimization

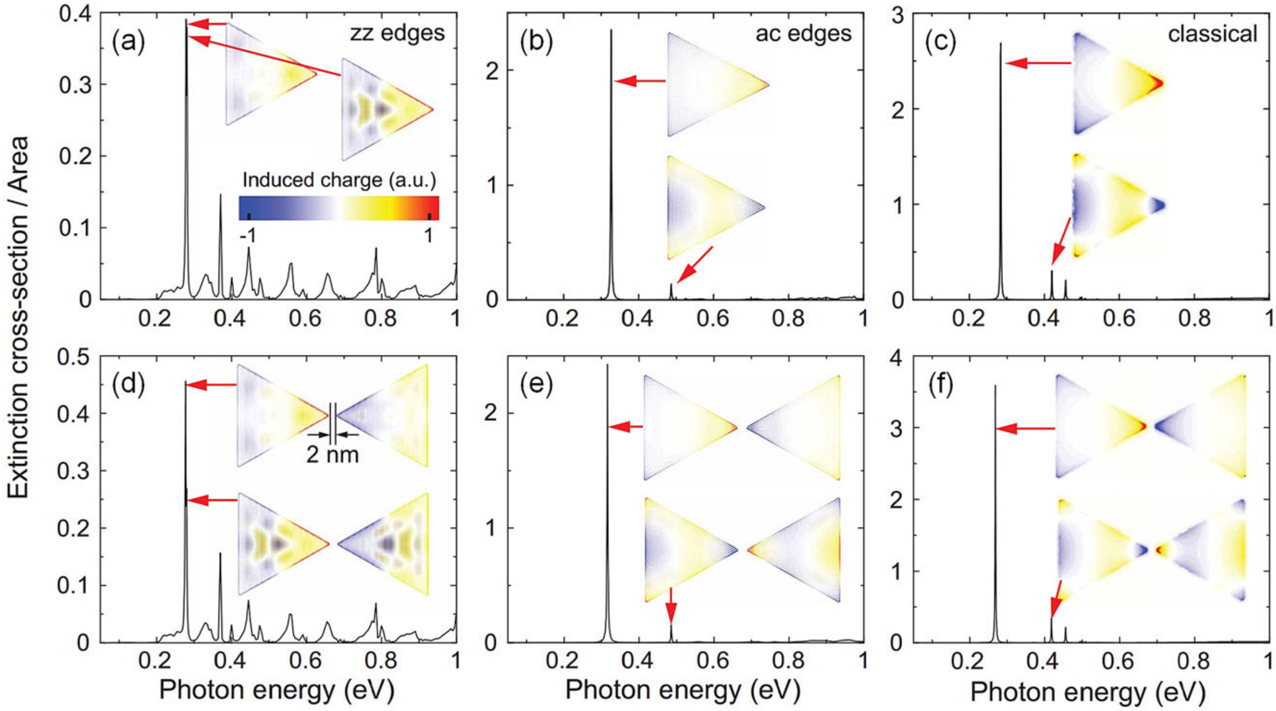

Figure 13 Extinction cross section as a function of photon energy and induced charges associated with the observed dominant plasmon features (shown by red arrows) for (a–c) individual graphene triangles and (d–f) bowtie graphene dimers. The quantum mechanical description (RPA) of (a,d) zz and (b,e) ac triangles is shown. The classical description is shown in (c,f). The triangle side length is $L = 20$ nm, the Fermi energy is $E_F = 0.4$ eV, and the intrinsic width is $\tau^{-1} = 1.6$ meV in all cases. Adapted with permission from Ref. [237]. Copyright (2013) American Physical Society.

algorithms [9, 246, 247]. There, hundreds or more systems are usually screened or iteratively studied and the efficiency of the method (in terms of computational time and memory) is crucial. It is therefore important to determine the figure of merit for which the system has to be optimized prior to selection of the method.

With the progress in nanofabrication and optical characterization methods, optical effects which call for modeling beyond Maxwell's equations in their classical form are now observed. In particular, novel materials such as graphene with a two-dimensional geometry appear in plasmonic devices. It has also been seen in Section 3 that quantum and nonlocal effects appear for nanostructures with nanometric and sub-nanometric features, and other nonlinear effects are generated with high optical intensities. An extremely accurate rendering of the geometries including their defects is required. A more precise modeling of the permittivities is a possible direction for future developments, which includes the details of structural properties, crystallinity, and complex dispersion. In other classes of active and optoelectronic devices such as lasers, solar cells, or photodetectors, the electrodynamics needs to be combined with transport properties and dynamics of charge carriers. The emerging field of plasmon-enhanced photocatalysis has many modeling challenges before it, which are related in particular to the mechanisms by which surface plasmons can induce chemical reactions on metal surfaces, or the mechanisms responsible for the transfer of charge from an excited nanoparticle to an adsorbate [54].

Received: 7 May 2015, **Revised:** 19 August 2015,
Accepted: 30 September 2015

Key words: Numerical simulations, nanophotonics, finite differences, finite elements, integral methods.

Benjamin Gallinet received a PhD degree in photonics in 2012 at the Swiss Federal Institute of Technology, Lausanne (EPFL). He now occupies the position of senior R&D engineer at CSEM SA where he is leading projects in the thin-film optics division, with the aim of enabling the transfer of nano-optical technologies to industry. His current research interests include nanophotonics and plasmonics.

Jérémy Butet received a PhD degree at the University of Lyon, France, in 2012. He joined the Nanophotonics and Metrology Laboratory (NAM) at the Swiss Federal Institute of Technology, Lausanne (EPFL) in 2012 as a postdoctoral researcher. He develops new experiments and models for nonlinear plasmonics. His current research interests include nanosciences, nanophotonics, nonlinear optics, and plasmonics.

Olivier J. F. Martin is Professor of Nanophotonics and Optical Signal Processing at the Swiss Federal Institute of Technology, Lausanne (EPFL), where he is head of the Nanophotonics and Metrology Laboratory and Director of the Doctoral Program in Photonics. His research interests focus on the interactions of electromagnetic fields with low-dimension systems, especially in the optical regime and with emphasis on plasmonics. He has authored more than 200 journal articles and holds a handful of patents and invention disclosures.

References

[1] B. E. A. Saleh and M. C. Teich; Fundamentals of Photonics, 2nd edition (Wiley, Hoboken, NJ, 2007).

[2] A. E. Siegman, IEEE J. Sel. Topics Quantum Electron. **6**, 1380–1388 (2000).

[3] F. K. Reinhart, Semicond. Sci Technol. **27**, 090206 (2012).

[4] M. D. Lukin, Rev. Mod. Phys. **75**, 457–472 (2003).

[5] H. Walther, B. T. H. Varcoe, B. G. Englert, and T. Becker, Rep. Prog. Phys. **69**, 1325–1382 (2006).

[6] T. J. Kippenberg and K. J. Vahala, Opt. Express **15**, 17172–17205 (2007).

[7] K. Sakoda, Optical Properties of Photonic Crystals (Springer, Berlin, 2005).

[8] J. D. Joannopoulos, S. G. Johnson, J. N. Winn, and R. D. Meade, Photonic Crystals: Molding the Flow of Light (Princeton University Press, Princeton, NJ, 2008).

[9] M. Minkov and V. Savona, Sci. Rep. **4**, 5124 (2014).

[10] T. F. Krauss, Nat. Photonics **2**, 448–450 (2008).

[11] B. Hecht, B. Sick, U. P. Wild, V. Deckert, R. Zenobi, O. J. F. Martin, and D. W. Pohl, J. Chem. Phys. **112**, 7761–7774 (2000).

[12] O. J. F. Martin, C. Girard, and A. Dereux, Phys. Rev. Lett. **74**, 526–529 (1995).

[13] J. A. Schuller, Z. Rashid, T. Taubner, and M. L. Brongersma, Phys. Rev. Lett. **99**, 107401 (2007).

[14] M. I. Stockman, Opt. Express **19**, 22029–22106 (2011).

[15] R. Esteban, T. V. Teperik, and J. J. Greffet, Phys. Rev. Lett. **104**, 026802 (2010).

[16] K. A. Willets and R. P. Van Duyne, Annu. Rev. Phys. Chem. **58**, 267–297 (2007).

[17] N. Yu and F. Capasso, Nat. Mater. **13**, 139–150 (2014).

[18] S. Sun, K. Y. Yang, C. M. Wang, T. K. Juan, W. T. Chen, C. Y. Liao, Q. He, S. Xiao, W. T. Kung, G. Y. Guo, L. Zhou, and D. P. Tsai, Nano Lett. **12**, 6223–6229 (2012).

[19] N. Yu, P. Genevet, M. A. Kats, F. Aieta, J. P. Tetienne, F. Capasso, and Z. Gaburro, Science **334**, 333–337 (2011).

[20] Y. Montelongo, J. O. Tenorio-Pearl, C. Williams, S. Zhang, W. I. Milne, and T. D. Wilkinson, Proc. Natl Acad. Sci. USA **111**, 12679–12683 (2014).

[21] F. M. Kahnert, J. Quant. Spectrosc. Radiat. Transfer **79–80**, 775–824 (2003).

[22] E. K. Miller, IEEE Trans. Antennas Propag. **30**, 1281–1305 (1988).

[23] V. Myroshnychenko, E. Carbó-Argibay, I. Pastoriza-Santos, J. Pérez-Juste, L. M. Liz-Marzán, and F. J. García de Abajo, Adv. Mater. **20**, 4288–4293 (2008).

[24] G. A. E. Vandenbosch; Computational Electromagnetics in Plasmonics, in Plasmonics Principles and Applications (InTech, 2012).

[25] J. Smajic, C. Hafner, L. Raguin, K. Tavzarashvili, and M. Mishrikey, J. Comput. Theor. Nanosci. **6**, 1–12 (2009).

[26] G. A. E. Vandenbosch, V. Volski, N. Verellen, and V. V. Moshchalkov, Radio Sci. **46**, RS0E02 (2011).

[27] M. R. Gonçalves, J. Phys. D: Appl. Phys. **47**, 213001 (2014).

[28] K. Han and C. H. Chang, Nanomaterials **4**, 87–128 (2014).

[29] X. Guo, Y. Ma, Y. Wang, and L. Tong, Nanowire plasmonic waveguides, circuits and devices. Laser Photonics Rev. **7**, 855–881 (2013).

[30] J. C. Weeber, J. R. Krenn, A. Dereux, B. Lamprecht, Y. Lacroute, and J. P. Goudonnet, Phys. Rev. B **64**, 045411 (2001).

[31] T. Sfez, E. Descrovi, L. Yu, D. Brunazzo, M. Quaglio, L. Dominici, W. Nakagawa, F. Michelotti, F. Giorgis, O. J. F. Martin, and H. P. Herzig, J. Opt. Soc. Am. B **27**, 1617–1625 (2010).

[32] Y. Fang, Z. Li, Y. Huang, S. Zhang, P. Nordlander, N. J. Halas, and H. Xu, Nano Lett. **10**, 1950–1954 (2010).

[33] S. Nauert, A. Paul, Y. R. Zhen, D. Solis, L. Vigderman, W. S. Chang, E. R. Zubarev, P. Nordlander, and S. Link, ACS Nano **8**, 572–580 (2014).

[34] Musa S. M., Computational Nanophotonics (CRC Press, 2014).

[35] P. Berini and I. De Leon, Nat. Photonics **6**, 16–24 (2012).

[36] N. J. Halas, S. Lal, W. S. Chang, S. Link, and P. Nordlander, Chem. Rev. **111**, 3913–3961 (2011).

[37] M. W. Knight, H. Sobhani, P. Nordlander, and N. J. Halas, Science **332**, 702–704 (2011).

[38] Q. Gan, F. J. Bartoli, and Z. H. Kafafi, Adv. Mater. **25**, 2377–2377 (2013).

[39] M. L. Brongersma, Y. Cui, and S. Fan, Nat. Mater. **13**, 451–460 (2014).

[40] G. Baffou, and R. Quidant, Thermo-plasmonics: using metallic nanostructures as nano-sources of heat. Laser Photonics Rev. **7**, 171–187 (2013).

[41] O. Neumann, A. S. Urban, J. Day, S. Lal, P. Nordlander, and N. J. Halas, ACS Nano **7**, 42–49 (2013).

[42] J. B. Herzog, M. W. Knight, and D. Natelson, Nano Lett. **14**, 499–503 (2014).

[43] N. Liu, M. L. Tang, M. Hentschel, H. Giessen, and A. P. Alivisatos, Nat. Mater. **10**, 631–636 (2011).

[44] C. F. Bohren and D. R. Huffman, Absorption and Scattering of Light by Small Particles (Wiley, 1983).

[45] K. Kumar, H. Duan, R. S. Hegde, S. C. W. Koh, J. N. Wei, and J. K. W. Yang, Nat. Nanotechnol. **7**, 557–561 (2012).

[46] A. B. Evlyukhin, S. M. Novikov, U. Zywietz, R. L. Eriksen, C. Reinhardt, S. I. Bozhevolnyi, and B. N. Chichkov, Nano Lett. **12**, 3749–3755 (2012).

[47] L. Cao, P. Fan, E. S. Barnard, A. M. Brown, and M. L. Brongersma, Nano Lett. **10**, 2649–2654 (2010).

[48] A. G. Curto, G. Volpe, T. H. Taminiau, M. P. Kreuzer, R. Quidant, and N. F. van Hulst, Science **329**, 930–933 (2010).

[49] A. Losquin, L. F. Zagonel, V. Myroshnychenko, B. Rodríguez-Gonzślez, M. Tencé, L. Scarabelli, J. Förstner, L. M. Liz-Marzán, F. J. García de Abajo, O. Stéphan, and M. Kociak, Nano Lett. **15**, 1229–1237 (2015).

[50] K. Lodewijks, N. Maccaferri, T. Pakizeh, R. K. Dumas, I. Zubritskaya, J. Åkerman, P. Vavassori, and A. Dmitriev, Nano Lett. **14**, 7207–7214 (2014).

[51] M. Kauranen and A. V. Zayats, Nat. Phys. **6**, 737–748 (2012).

[52] M. S. Tame, K. R. McEnery, S. K. Ozdemir, J. Lee, S. A. Maier, and M. S. Kim, Nat. Phys. **9**, 329–340 (2013).

[53] M. Jablan, H. Buljan, and M. Soljačić, Phys. Rev. B **80**, 245435 (2009).

[54] S. Linic, U. Aslam, C. Boerigter, and M. Morabito, Nat. Mater. **14**, 567–576 (2015).

[55] J. M. Montgomery, T. W. Lee, and S. K. Gray, J. Phys.: Condens. Matter **20**, 323201 (2008).

[56] A. Taflove and S. C. Hagness, Computational Electrodynamics: The Finite-Difference Time-Domain Method (Artech House, Boston, MA, 2005).

[57] K. Yee, IEEE Trans. Antennas Propag. **14**, 302–307 (1966).

[58] R. F. Remis, J. Comput. Phys. **230**, 1382–1386 (2011).

[59] P. Monk, IEEE Trans. Magn. **30**, 3200–3203 (1994).

[60] S. Gedney, F. Lansing, and D. Rascoe, IEEE Trans. Microw. Theory Techn. **44**, 1393–1400 (1996).

[61] T. Wriedt and U. Comberg, J. Quant. Spectrosc. Radiat. Transfer **60**, 411–423 (1998).

[62] B. Gallinet, J. Kupec, B. Witzigmann, and M. A. Dupertuis, J. Opt. Soc. Am. B **27**, 1364–1380 (2010).

[63] J. Jin, Finite Element Method in Electromagnetics (Wiley, 2002).

[64] J. P. Berenger, J. Comput. Phys. **114**, 185–200 (1994).

[65] T. Weiland, A discretization method for the solution of Maxwell's equations for six-component fields, Electronics and Communications AEÜ **31**, 116–120 (1977).

[66] W. C. Chew and W. H. Weedon, Microwave Opt. Technol. Lett. **7**, 599–604 (1994).

[67] Z. S. Sacks, D. M. Kingsland, R. Lee, and J. F. Lee, IEEE Trans. Antennas Propag. **43**, 1460–1463 (1995).

[68] A. F. Oskooi, L. Zhang, Y. Avniel, and S. G. Johnson, Opt. Express **16**, 11376–11392 (2008).

[69] S. A. Maier, Plasmonics: Fundamentals and Applications (Springer Science, 2007).

[70] D. F. Kelley and R. J. Lubbers, IEEE Trans. Antennas Propag. **44**, 792–797 (1996).

[71] M. Okoniewski and E. Okoniewska, IEEE Microw. Guided Wave Lett. **3**, 121–123 (1997).

[72] G. Mur, IEEE Trans. Electromagn. Compat. **23**, 377–382 (1981).

[73] S. K. Gray and T. Kupka, Phys. Rev. B **68**, 045415 (2003).

[74] L. J. E. Anderson, Y. R. Zhen, C. M. Payne, P. Nordlander, and J. H. Hafner, Nano Lett. **13**, 6256–6261 (2013).

[75] A. Oskooi and S. G. Johnson, Meep fdtd simulation software package, http://ab-initio.mit.edu/wiki/index.php/Meep, Accessed: 14.08.2015.

[76] J. C. Nédélec, Numer. Meth. **35**, 315–341 (1980).

[77] G. Warren and W. Scott, IEEE Trans. Antennas Propag. **44**, 317–320 (1996).

[78] R. Kappeler, D. Erni, C. Xudong, and L. Novotny, J. Comput. Theor. Nanosci. **4**, 686–691 (2007).

[79] D. Barchiesi, C. Girard, O. J. F. Martin, D. Van-Labeke, and D. Courjon, Phys. Rev. E **54**, 4285–4292 (1996).

[80] Y. J. Lu, J. Kim, H. Y. Chen, C. Wu, N. Dabidian, C. E. Sanders, C. Y. Wang, M. Y. Lu, B. H. Li, X. Qiu, W. H. Chang, L. J. Chen, G. Shvets, C. K. Shih, and S. Gwo, Science **337**, 450–453 (2012).

[81] Q. Zhang, G. Li, X. Liu, F. Qian, Y. Li, T. Chien Sum, C. M. Lieber, and Q. Xiong, Nat. Commun. **5**, 4953 (2014).

[82] W. Zhang, L. Huang, C. Santschi, and O. J. F. Martin, Nano Lett. **10**, 1006–1011 (2010).

[83] M. F. Wong, O. Picon, and V. F. Hanna, IEEE Trans. Magn. **32**, 1393–1396 (1996).

[84] Z. Lou and J. M. Jin, IEEE Trans. Antennas Propag. **54**, 1850–1862 (2006).

[85] Z. Lou and J. M. Jin, IEEE Trans. Antennas Propag. **54**, 2990–2999 (2006).

[86] T. Rylander and A. Bondeson, Comput. Phys. Commun. **125**, 75–82 (2000).

[87] K. Busch, M. König, and J. Niegemann, Laser Photonics Rev. **5**, 773–809 (2011).

[88] J. Niegemann, W. Pernice, and K. Busch, J. Opt. A **11**, 114015 (2009).

[89] J. Niegemann, M. König, K. Stannigel, and K. Busch, Photonic Nanostruct. **7**, 2–11 (2009).

[90] O. J. F. Martin and N. B. Piller, Phys. Rev. E **58**, 3909–3915 (1998).

[91] B. T. Draine and P. J. Flatau, J. Opt. Soc. Am. A **11**, 1491–1499 (1994).

[92] V. V. Varadan, A. Lakhtakia, and V. K. Varadan, IEEE Trans. Antennas Propag. **37**, 800–802 (1989).

[93] J. Van Kranendonk and J. E. Sipe, Foundations of the Macroscopic Electromagnetic Theory of Dielectric Media, Progress in Optics 15 (Elsevier, 1977).

[94] N. B. Piller and O. J. F. Martin, IEEE Trans. Antennas Propag. **46**, 1126–1137 (1998).

[95] P. Gay-Balmaz and O. J. F. Martin, Comput. Phys. Commun. **144**, 111–120 (2002).

[96] J. P. Kottmann and O. J. F. Martin, IEEE Trans. Antennas Propag. **48**, 1719–1726 (2000).

[97] M. A. Yurkin and M. Kahnert, J. Quant. Spectrosc. Radiat. Transfer **123**, 176–183 (2013).

[98] P. J. Flatau, Opt. Lett. **22**, 1205–1207 (1997).

[99] M. Paulus and O. J. F. Martin, J. Opt. Soc. Am. A **18**, 854–861 (2001).

[100] M. Paulus, P. Gay-Balmaz, and O. J. F. Martin, Phys. Rev. E **62**, 5797–5807 (2000).

[101] M. Paulus, H. Schmid, B. Michel, and O. J. F. Martin, Microelectron. Eng. **57–58**, 109–116 (2001).

[102] H. Schmid, H. Biebuyck, B. Michel, and O. J. F. Martin, Appl. Phys. Lett. **72**, 2379–2381 (1998).

[103] A. D. Yaghjian, Proc. IEEE **68**, 248–263 (1980).

[104] J. D. Jackson, Classical Electrodynamics, 3 edition (Wiley, 1998).

[105] B. T. Draine, Astrophys. J. **333**, 848–872 (1988).

[106] D. Gutkowicz-Krusin and B. Draine, arXiv:astro-ph/0403082 (2004).

[107] W. H. Press, S. A. Teukolsky, W. T. Vetterling, and B. P. Flannery, Numerical Recipes: The Art of Scientific Computing, 3rd edition (Cambridge University Press, Cambridge, 2007).

[108] J. J. Goodman, B. T. Draine, and P. J. Flatau, Opt. Lett. **16**, 1198–1200 (1991).

[109] B. T. Draine, Ddscat light scattering code, http://www.ddscat.org/, Accessed: 22.04.2015.

[110] P. C. Chaumet, A. Rahmani, and G. W. Bryant, Phys. Rev. B **67**, 165404 (2003).
[111] B. T. Draine and P. J. Flatau, J. Opt. Soc. Am. A **25**, 2693–2703 (2008).
[112] P. C. Chaumet and A. Sentenac, J. Quant. Spectrosc. Radiat. Transfer **110**, 409–414 (2009).
[113] I. Stevanovic, P. Crespo-Valero, K. Blagovic, F. Bongard, and J. R. Mosig, IEEE Trans. Microw. Theory Techn. **54**, 3688–3697 (2006).
[114] E. N. Economou, Green's Functions in Quantum Mechanics, 3rd edition (Springer, Berlin, 2006).
[115] R. E. Kleinman, G. F. Roach, and P. M. Vandenberg, J. Opt. Soc. Am. A **7**, 890–897 (1990).
[116] O. J. F. Martin, A. Dereux, and C. Girard, J. Opt. Soc. Am. A **11**, 1073–1080 (1994).
[117] A. M. Kern and O. J. F. Martin, J. Opt. Soc. Am. A **26**, 732–740 (2009).
[118] J. M. Taboada, J. Rivero, F. Obelleiro, M. G. Araujo, and L. Landesa, J. Opt. Soc. Am. A **28**, 1341–1348 (2011).
[119] F. J. García de Abajo and A. Howie, Phys. Rev. B **65**, 115418 (2002).
[120] R. F. Harrington, Field Computation by Moment Methods (Macmillan, 1968).
[121] S. Rao, D. Wilton, and A. Glisson, IEEE Trans. Antennas Propag. **30**(May), 409–418 (1982).
[122] M. G. Araújo, J. M. Taboada, D. M. Solís, J. Rivero, L. Landesa, and F. Obelleiro, Opt. Express **20**, 9161–9171 (2012).
[123] C. Forestiere, A. Capretti, and G. Miano, J. Opt. Soc. Am. B **30**, 2355–2364 (2013).
[124] T. K. Wu and L. L. Tsai, Radio Sci. **12**, 709–718 (1977).
[125] M. S. Yeung and E. Barouch, Proc. SPIE **3051**, 509–521 (1997).
[126] X. Q. Sheng, J. M. Jin, J. M. Song, W. C. Chew, and C. C. Lu, IEEE Trans. Antennas Propag. **46**, 1718–1726 (1998).
[127] P. Ylä-Oijala and M. Taskinen, IEEE Trans. Antennas Propag. **53**, 1168–1173 (2005).
[128] A. M. Kern and O. J. F. Martin, Nano Lett. **11**, 482–487 (2011).
[129] A. M. Kern, A. J. Meixner, and O. J. F. Martin, ACS Nano **6**, 9828–9836 (2012).
[130] Y. P. Chen, W. E. I. Sha, W. C. H. Choy, L. Jiang, and W. C. Chew, Opt. Express **20**, 20210–20221 (2012).
[131] B. Gallinet and O. J. F. Martin, Photonic Nanostruct. **8**, 278–284 (2010).
[132] B. Gallinet, A. M. Kern, and O. J. F. Martin, J. Opt. Soc. Am. A **27**, 2261–2271 (2010).
[133] B. Gallinet and O. J. F. Martin, Opt. Express **19**, 22167–22175 (2011).
[134] B. Gallinet, T. Siegfried, H. Sigg, P. Nordlander, and O. J. F. Martin, Nano Lett. **13**, 497–503 (2013).
[135] M. G. Araújo, J. M. Taboada, J. Rivero, D. M. Solís, and F. Obelleiro, Opt. Lett. **37**, 416–418 (2012).
[136] D. M. Solís, J. M. Taboada, F. Obelleiro, L. M. Liz-Marzán, and F. J. García de Abajo, ACS Nano **8**, 7559–7570 (2014).
[137] K. Zhao, M. N. Vouvakis, and J. F. Lee, IEEE Trans. Electromagn. Compat. **47**, 763–773 (2005).
[138] H. Wallén and J. Sarvas, Prog. Electromagn. Res. **55**, 47–78 (2005).
[139] J. Aizpurua, P. Hanarp, D. S. Sutherland, M. Käll, G. W. Bryant, and F. J. García de Abajo, Phys. Rev. Lett. **90**, 057401 (2003).
[140] V. Myroshnychenko, J. Rodriguez-Fernandez, I. Pastoriza-Santos, A. M. Funston, C. Novo, P. Mulvaney, L. M. Liz-Marzán, and F. J. García de Abajo, Chem. Soc. Rev. **37**, 1792–1805 (2008).
[141] G. Baffou, R. Quidant, and F. J. García de Abajo, ACS Nano **4**, 709–716 (2010).
[142] U. Hohenester and A. Trügler, Comput. Phys. Commun. **183**, 370–381 (2012).
[143] M. I. Mishchenko, L. D. Travis, and D. W. Mackowski, J. Quant. Spectrosc. Radiat. Transfer **55**, 535–575 (1996).
[144] R. Boyack and E. C. Le Ru, Phys. Chem. Chem. Phys. **11**, 7398–7405 (2009).
[145] N. G. Khlebstov, J. Quant. Spectrosc. Radiat. Transfer **123**, 184–217 (2013).
[146] H. C., The Generalized Multipole Technique for Computational Electromagnetics (Artech House, Boston, MA, 1990).
[147] C. Hafner, Post-Modern Electromagnetics Using Intelligent Maxwell Solvers (Wiley, Chichester, UK, 1999).
[148] F. J. García de Abajo, Phys. Rev. B **60**, 6086–6102 (1999).
[149] M. G. Moharam, E. B. Grann, D. A. Pommet, and T. K. Gaylord, J. Opt. Soc. Am. A **12**, 1068–1076 (1995).
[150] P. Lalanne and M. P. Jurek, J. Mod. Opt. **45**, 1357–1374 (1998).
[151] S. Massenot, R. Chevallier, J. L. de Bougrenet de la Tocnaye, and O. Parriaux, Opt. Commun. **275**, 318–323 (2007).
[152] P. Lalanne and G. M. Morris, J. Opt. Soc. Am. A **13**, 779–784 (1996).
[153] A. Dhawan, M. Canva, and T. Vo-Dinh, Opt. Express **19**, 787–813 (2011).
[154] J. Chandezon, D. Maystre, and G. Raoult, J. Opt.-Nouv. Rev. Opt. **11**, 235–241 (1980).
[155] U. Leonhard and P. T. G., Transformation Optics and the Geometry of Light, Progress in Optics 53 (Elsevier, 2009).
[156] L. Xu and H. Chen, Nat. Photonics **9**, 15–23 (2015).
[157] R. W. Boyd, Nonlinear Optics (Academic Press, New York, 1992).
[158] K. Imura, T. Nagahara, and H. Okamoto, J. Phys. Chem. B **109**, 13214–13220 (2005).
[159] P. Biagioni, M. Celebrano, M. Savoini, G. Grancini, D. Brida, S. Mátéfi-Tempfli, M. Mátéfi-Tempfli, L. Duò, B. Hecht, G. Cerullo, and M. Finazzi, Phys. Rev. B **80**, 045411 (2009).
[160] X. F. Jiang, Y. Pan, C. Jiang, T. Zhao, P. Yuan, T. Venkatesan, and Q. H. Xu, J. Phys. Chem. Lett. **4**, 1634–1638 (2013).
[161] D. S. Wang, F. Y. Hsu, and C. W. Lin, Opt. Express **17**, 11350–11359 (2009).
[162] H. Wang, T. B. Huff, D. A. Zweifel, W. He, P. S. Low, A. Wei, and J. X. Cheng, Proc. Natl Acad. Sci. USA **102**, 15752–15756 (2005).
[163] G. Bachelier, J. Butet, I. Russier-Antoine, C. Jonin, E. Benichou, and P. F. Brevet, Phys. Rev. B **82**, 235403 (2010).
[164] F. X. Wang, F. J. Rodriguez, W. M. Albers, R. Ahorinta, J. E. Sipe, and M. Kauranen, Phys. Rev. B **80**, 233402 (2009).
[165] G. Bachelier, I. Russier-Antoine, E. Benichou, C. Jonin, and P. F. Brevet, J. Opt. Soc. Am. B **25**, 955–960 (2008).

[166] J. Butet, G. Bachelier, I. Russier-Antoine, C. Jonin, E. Benichou, and P. F. Brevet, , Phys. Rev. Lett. **105**, 077401 (2010).
[167] Y. Zhang, N. K. Grady, C. Ayala-Orozco, and N. J. Halas, Nano Lett. **11**, 5519–5523 (2011).
[168] J. Makitalo, S. Suuriniemi, and M. Kauranen, Opt. Express **19**, 23386–23399 (2011).
[169] J. Mäkitalo, S. Suuriniemi, and M. Kauranen, J. Opt. Soc. Am. A **31**, 2821–2832 (2014).
[170] Y. Zeng, W. Hoyer, J. Liu, S. W. Koch, and J. V. Moloney, Phys. Rev. B **79**, 235109 (2009).
[171] A. Benedetti, M. Centini, C. Sibilia, and M. Bertolotti, J. Opt. Soc. Am. B **27**, 408–416 (2010).
[172] C. Ciracì, E. Poutrina, M. Scalora, and D. R. Smith, Phys. Rev. B **86**, 115451 (2012).
[173] D. de Ceglia, M. A. Vincenti, C. D. Angelis, A. Locatelli, J. W. Haus, and M. Scalora, Opt. Express **23**, 1715–1729 (2015).
[174] T. Laroche, F. I. Baida, and D. V. Labeke, J. Opt. Soc. Am. B **22**, 1045–1051 (2005).
[175] A. Benedetti, M. Centini, M. Bertolotti, and C. Sibilia, Opt. Express **19**, 26752–26767 (2011).
[176] J. Butet, K. Thyagarajan, and O. J. F. Martin, Nano Lett. **13**, 1787–1792 (2013).
[177] J. Butet, B. Gallinet, K. Thyagarajan, and O. J. F. Martin, J. Opt. Soc. Am. B **30**, 2970–2979 (2013).
[178] J. Butet and O. J. F. Martin, Opt. Express **22**, 29693–29707 (2014).
[179] M. Lippitz, M. A. van Dijk, and M. Orrit, Nano Lett. **5**, 799–802 (2005).
[180] M. Hentschel, T. Utikal, H. Giessen, and M. Lippitz, Nano Lett. **12**, 3778–3782 (2012).
[181] B. Metzger, T. Schumacher, M. Hentschel, M. Lippitz, and H. Giessen, ACS Photonics pp. 471–476 (2014).
[182] J. B. Lassiter, X. Chen, X. Liu, C. Ciraci, T. B. Hoang, S. Larouche, S. H. Oh, M. H. Mikkelsen, and D. R. Smith, ACS Photonics **1**, 1212–1217 (2014).
[183] X. Liu, S. Larouche, P. Bowen, and D. R. Smith, Opt. Express **23**, 19565–19574 (2015).
[184] T. A. Luce, W. Hubner, and K. H. Bennemann, Z. Phys. B **102**, 223–232 (1997).
[185] P. Ginzburg, A. V. Krasavin, G. A. Wurtz, and A. V. Zayats, ACS Photonics **2**, 8–13 (2015).
[186] S. H. Chang and A. Taflove, Opt. Express **12**, 3827–3833.
[187] W. Zhou, M. Dridi, J. Y. Suh, C. H. Kim, D. T. Co, M. R. Wasielewski, G. C. Schatz, and T. W. Odom, Nat. Nanotechnol. **8**, 506–511 (2013).
[188] A. Fang, T. Koschny, M. Wegener, and C. M. Soukoulis, Phys. Rev. B **79**, 241104 (2009).
[189] T. Lanz, B. Ruhstaller, C. Battaglia, and C. Ballif, J. Appl. Phys. **110**, 033111 (2011).
[190] U. Kreibig and M. Vollmer, Optical Properties of Metal Clusters (Springer-Verlag, Berlin, 1995).
[191] P. B. Johnson and R. W. Christy, Phys. Rev. B **6**, 4370–4379 (1972).
[192] S. Gao and Z. Yuan, Phys. Rev. B **72**, 121406 (2005).
[193] B. B. Dasgupta and R. Fuchs, Phys. Rev. B **24**, 554–561 (1981).
[194] R. Fuchs and F. Claro, Phys. Rev. B **35**, 3722–3727 (1987).
[195] R. Rojas, F. Claro, and R. Fuchs, Phys. Rev. B **37**, 6799–6807 (1988).
[196] N. D. Mermin, Phys. Rev. B **1**, 2362–2363 (1970).
[197] R. H. Ritchie and A. L. Marusak, Surf. Sci. **4**, 234–240 (1966).
[198] F. J. García de Abajo, J. Phys. Chem. C **112**, 17983–17987 (2008).
[199] C. David and F. J. García de Abajo, J. Phys. Chem. C **115**, 19470–19475 (2011).
[200] J. M. McMahon, S. K. Gray, and G. C. Schatz, Nano Lett. **10**, 3473–3481 (2010).
[201] A. Wiener, A. I. Fernández-Domínguez, A. P. Horsfield, J. B. Pendry, and S. A. Maier, Nano Lett. **12**, 3308–3314 (2012).
[202] G. Toscano, S. Raza, A. P. Jauho, N. A. Mortensen, and M. Wubs, Opt. Express **20**, 4176–4188 (2012).
[203] T. V. Teperik, N. P., J. Aizpurua, and A. G. Borisov, Phys. Rev. Lett. **110**, 263901 (2013).
[204] W. Yan, N. A. Mortensen, and M. Wubs, Phys. Rev. B **88**, 155414 (2013).
[205] A. Zangwill and P. Soven, Phys. Rev. A **21**, 1561–1572 (1980).
[206] W. Ekardt, Phys. Rev. B **31**, 6360–6370 (1985).
[207] M. J. Puska, R. M. Nieminen, and M. Manninen, Phys. Rev. B **31**, 3486–3495 (1985).
[208] D. E. Beck, Phys. Rev. B **35**, 7325–7333 (1987).
[209] E. Cottancin, J. Lermé, M. Gaudry, M. Pellarin, J. L. Vialle, M. Broyer, B. Prével, M. Treilleux, and P. Mélinon, Phys. Rev. B **62**, 5179–5185 (2000).
[210] L. Jensen, C. M. Aikens, and G. C. Schatz, Chem. Soc. Rev. **37**, 1061–1073 (2008).
[211] E. Townsend and G. W. Bryant, Nano Lett. **12**, 429–434 (2012).
[212] E. Prodan and P. Nordlander, Nano Lett. **3**, 543–547 (2003).
[213] E. Prodan, P. Nordlander, and N. J. Halas, Nano Lett. **3**, 1411–1415 (2003).
[214] H. E. Johnson and C. M. Aikens, J. Phys. Chem. A **113**, 4445–4450 (2009).
[215] J. Zuloaga, E. Prodan, and P. Nordlander, ACS Nano **4**, 5269–5276 (2010).
[216] K. J. Savage, M. M. Hawkeye, R. Esteban, A. G. Borisov, J. Aizpurua, and J. J. Baumberg, Nature **491**, 574–577 (2012).
[217] R. Esteban, A. G. Borisov, P. Nordlander, and J. Aizpurua, Nat. Commun. **3**, 825 (2012).
[218] J. A. Scholl, A. García-Etxarri, A. L. Koh, and J. A. Dionne, Nano Lett. **13**, 564–569 (2013).
[219] L. Wu, H. Duan, P. Bai, M. Bosman, J. K. W. Yang, and E. Li, ACS Nano **7**, 707–716 (2013).
[220] J. Zuloaga, E. Prodan, and P. Nordlander, Nano Lett. **9**, 887–891 (2009).
[221] M. Zapata, Ángela S. Camacho Beltrán, A. G. Borisov, and J. Aizpurua, Opt. Express **23**, 8134–8149 (2015).
[222] G. Hajisalem, M. S. Nezami, and R. Gordon, Nano Lett. **14**, 6651–6654 (2014).
[223] J. W. Haus, D. de Ceglia, M. A. Vincenti, and M. Scalora, J. Opt. Soc. Am. B **31**, A13–A19 (2014).
[224] R. Esteban, G. Aguirregabiria, A. G. Borisov, Y. M. Wang, P. Nordlander, G. W. Bryant, and J. Aizpurua, ACS Photonics **2**, 295–305 (2015).
[225] K. S. Novoselov, A. K. Geim, S. V. Morozov, D. Jiang, Y. Zhang, S. V. Dubonos, I. V. Grigorieva, and A. A. Firsov, Science **306**, 666–669 (2004).

[226] A. N. Grigorenko, M. Polini, and K. S. Novoselov, Nat. Photonics **6**, 749–758 (2012).
[227] Q. Bao and K. P. Loh, ACS Nano **6**, 3677–3694 (2012).
[228] F. J. García de Abajo, ACS Photonics **1**, 135–152 (2014).
[229] A. H. Castro Neto, F. Guinea, N. M. R. Peres, K. S. Novoselov, and A. K. Geim, Rev. Mod. Phys. **81**, 109–162 (2009).
[230] K. F. Mak, M. Y. Sfeir, Y. Wu, C. H. Lui, J. A. Misewich, and T. F. Heinz, Phys. Rev. Lett. **101**, 196405 (2008).
[231] F. H. L. Koppens, D. E. Chang, and F. J. García de Abajo, Nano Lett. **11**, 3370–3377 (2011).
[232] Z. Fang, S. Thongrattanasiri, A. Schlather, Z. Liu, L. Ma, Y. Wang, P. M. Ajayan, P. Nordlander, N. J. Halas, and F. J. García de Abajo, ACS Nano **7**, 2388–2395 (2013).
[233] L. Ju, B. Geng, J. Horng, C. Girit, M. Martin, Z. Hao, H. A. Bechtel, X. Liang, A. Zettl, Y. Ron Shen and F. Wang, Nat. Nanotechnol. **6**, 630–634 (2011).
[234] J. Christensen, A. Manjavacas, S. Thongrattanasiri, F. H. L. Koppens, and F. J. García de Abajo, ACS Nano **6**, 431–440 (2012).
[235] Z. Fang, Y. Wang, A. E. Schlather, Z. Liu, P. M. Ajayan, F. J. García de Abajo, P. Nordlander, X. Zhu, and N. J. Halas, Nano Lett. **14**, 299–304 (2014).
[236] H. Yan, F. Xia, Z. Li, and P. Avouris, New J. Phys. **14**, 125001 (2012).
[237] S. Thongrattanasiri and F. J. García de Abajo, Phys. Rev. Lett. **110**, 187401 (2013).
[238] A. Fallahi and J. Perruisseau-Carrier, Phys. Rev. B **86**, 195408 (2012).
[239] S. Thongrattanasiri, F. H. L. Koppens, and F. J. García de Abajo, Phys. Rev. Lett. **108**, 047401 (2012).
[240] E. H. Hwang and S. Das Sarma, Phys. Rev. B **75**, 205418 (2007).
[241] B. Wunsch, T. Stauber, F. Sols, and F. Guinea, New J. Phys. **8**, 318 (2006).
[242] L. A. Falkovsky and S. S. Pershoguba, Phys. Rev. B **76**, 153410 (2007).
[243] L. A. Falkovsky and A. A. Varlamov, Eur. Phys. J. B **56**, 281–284 (2007).
[244] P. N. Romanets and F. T. Vasko, Phys. Rev. B **81**, 085421 (2010).
[245] L. M. Malard, K. F. Mak, A. H. C. Neto, N. M. R. Peres, and T. F. Heinz, New J. Phys. **15**, 015009 (2013).
[246] C. Forestiere, A. J. Pasquale, A. Capretti, G. Miano, A. Tamburrino, S. Y. Lee, B. M. Reinhard, and L. Dal Negro, Nano Lett. **12**, 2037–2044 (2012).
[247] J. A. Bossard, L. Lin, S. Yun, L. Liu, D. H. Werner, and T. S. Mayer, ACS Nano **8**, 1517–1524 (2014).
[248] X. Wu, S. K. Gray, and M. Pelton, Opt. Express **18**, 23633–23645 (2010).